Princeton Plasma Physics Laboratory

PPPL-

PPPL-

PRINCETON PLASMA PHYSICS LABORATORY

Princeton Plasma Physics Laboratory
Report Disclaimers

Full Legal Disclaimer

This report was prepared as an account of work sponsored by an agency of the United States Government. Neither the United States Government nor any agency thereof, nor any of their employees, nor any of their contractors, subcontractors or their employees, makes any warranty, express or implied, or assumes any legal liability or responsibility for the accuracy, completeness, or any third party's use or the results of such use of any information, apparatus, product, or process disclosed, or represents that its use would not infringe privately owned rights. Reference herein to any specific commercial product, process, or service by trade name, trademark, manufacturer, or otherwise, does not necessarily constitute or imply its endorsement, recommendation, or favoring by the United States Government or any agency thereof or its contractors or subcontractors. The views and opinions of authors expressed herein do not necessarily state or reflect those of the United States Government or any agency thereof.

Trademark Disclaimer

Reference herein to any specific commercial product, process, or service by trade name, trademark, manufacturer, or otherwise, does not necessarily constitute or imply its endorsement, recommendation, or favoring by the United States Government or any agency thereof or its contractors or subcontractors.

PPPL Report Availability

Princeton Plasma Physics Laboratory:

http://www.pppl.gov/techreports.cfm

Office of Scientific and Technical Information (OSTI):

http://www.osti.gov/bridge

Related Links:

U.S. Department of Energy

Office of Scientific and Technical Information

Fusion Links

FES Joint Facilities Research Milestone 2011 – NSTX final report

By R. Maingi, D.P. Boyle, J. M. Canik, A. Diallo, and the NSTX Team

Annual Target:

Experiment:

Improve the understanding of the physics mechanisms responsible for the structure of the pedestal and compare with the predictive models described in the companion theory milestone. Perform experiments to test theoretical physics models in the pedestal region on multiple devices over a broad range of plasma parameters (e.g., collisionality, beta, and aspect ratio). Detailed measurements of the height and width of the pedestal will be performed augmented by measurements of the radial electric field. The evolution of these parameters during the discharge will be studied. Initial measurements of the turbulence in the pedestal region will also be performed to improve understanding of the relationship between edge turbulent transport and pedestal structure.

Theory:

A focused analytic theory and computational effort, including large-scale simulations, will be used to identify and quantify relevant physics mechanisms controlling the structure of the pedestal. The performance of future burning plasmas is strongly correlated with the pressure at the top of the edge transport barrier (or pedestal height). Predicting the pedestal height has proved challenging due to a wide and overlapping range of relevant spatiotemporal scales, geometrical complexity, and a variety of potentially important physics mechanisms. Predictive models will be developed and key features of each model will be tested against observations, to clarify the relative importance of various physics mechanisms, and to make progress in developing a validated physics model for the pedestal height.

Quarter 4 Milestone

Planned experiments will have been carried out. Data will be documented.

Key features of different theoretical models will be tested against observations, to clarify the relative importance of various physics mechanisms, and to make progress in developing a validated physics model for the pedestal height.

A preliminary assessment of the implications for ITER will be undertaken.

FES Joint Facilities Research Milestone 2011 – NSTX final report

Completion of 4th Quarter Milestone – Executive Summary

The NSTX portions of the targeted goals for the fourth quarter and for the entire year were achieved, as documented below. The research was focused in two main areas: pedestal and stability characteristics in ELMy H-mode, and in the transition from ELMy to ELM-free H-mode enabled via lithium wall coatings. Experiments supporting each area were conducted in early FY2011, and the analysis was completed during the remainder of the FY. The focus of our theory/experiment comparison was on peeling/ballooning stability analysis with ELITE; in addition, we performed simple estimates evaluating paleoclassical transport. Finally additional work was done to characterize the profiles and turbulence in Enhanced Pedestal H-modes.

We analyzed the evolution of pedestal, height, width, and gradients, as well as density fluctuations, during the inter-ELM cycle as a function of plasma current, I_p. Our list of high level findings include:

1. The pedestal pressure height P_{tot}^{ped} saturates only in the last 30% of the ELM cycle at low and intermediate I_p, and not at all at the high $I_p > 1$ MA.

2. The P_{tot}^{ped} increases ~ quadratically with I_p, and increases with lower divertor triangularity δ_l, but appears to be independent of toroidal field B_t.

3. The pedestal pressure width in physical space, P_{tot}^{width}, increases during the ELM cycle, and appears to be independent of I_p.

4. The pedestal pressure width in normalized poloidal flux (ψ_N) space, Δ, increases as the square root of pedestal β normalized to the poloidal magnetic field, β_θ^{ped}; the leading coefficient is notably however higher than other devices.

5. The maximum pressure gradient saturates early in the ELM cycle, but increases with I_p.

6. A coherent density fluctuation strongly increasing at the plasma edge was observed on reflectometry; the amplitude of this fluctuation was a maximum after the ELM crash, and it decayed during the rest of the ELM cycle.

We analyzed the evolution of global and edge plasma parameters during scans of increasing lithium deposition, during which plasmas transitioned slowly from ELMy to ELM-free. The main findings include:

FES Joint Facilities Research Milestone 2011 – NSTX final report

1. Divertor recycling light and profile peaking factors decreased with increasing lithium evaporation between discharges; the cross-field electron thermal diffusivity χ_e at $\rho=0.7$ showed a continuous decrease with lithium evaporation.

2. Edge χ_e and particle diffusivity D near the top of the pedestal decreased with increasing lithium evaporation. Effectively the minimum level of transport in the steep gradient region of the H-mode barrier was extended inward from ψ_N = 0.94 to ψ_N =0.8.

3. Density fluctuations measured from reflectometry and high-k scattering at the top of the pedestal were reduced by $\sim$ 90%.

4. The ratio of T_e to n_e scale lengths, η_e, was close to 1, in the region where electron temperature gradient modes are expected to be destabilized, i.e. they may be responsible for the stiff T_e profiles. On the other hand, the magnitude and profile of the inferred electron thermal transport diffusivities from ψ_N = 0.8-1 was remarkably close to that predicted from paleoclassical transport theory for the with-lithium discharges.

5. Edge stability calculations with ELITE of this transition showed that the ELMy discharges were all near the kink/peeling boundary, far from the ballooning boundary; ELM-free discharges were removed from the kink/peeling stability limit.

6. The critical parameters that separated ELMy and ELM-free operation were the density and pressure profile width and symmetry point locations; large widths and symmetry points farther from the separatrix correlated with ELM-free discharges.

These results encourage the continued use of lithium for wall conditioning and edge studies in NSTX-Upgrade. It is likely that studies that target the reason for the confinement improvement, including the continuous dependence on the pre-discharge lithium evaporation amount, will receive initial priority. Moreover the location of NSTX discharges on the kink/peeling side of the peeling-ballooning diagram parallels that expected in ITER. One qualitative conclusion then is that control of the density profile could be critical for ELM control in ITER, just as it appears to be in NSTX.

FES Joint Facilities Research Milestone 2011 – NSTX final report

The main body of this report is divided into two main sections: ELMy H-mode, and the ELMy to ELM-free transition with lithium coatings. In addition, a small section on advances in Enhanced Pedestal H-mode characterization is included, as that regime offers the prospect of separated particle and thermal transport channels.

I. ELMy H-mode analysis

A defining feature of the high confinement or "H-mode" operational scenario is the existence of a transport barrier near the plasma boundary; this localized region of low transport is characterized by an increase in local gradients[1]. The plasma profiles thus develop a stairstep or "pedestal" shape, which is commonly referred to as the "H-mode pedestal". This pedestal can be quite narrow in width and is interpreted as the interface between two regions during H-mode operation: the core plasma and the scrape-off layer. These two regions are governed by different physical mechanisms inherent in the wide range of spatial and temporal scales and also in the presence of sources and sinks of particles.

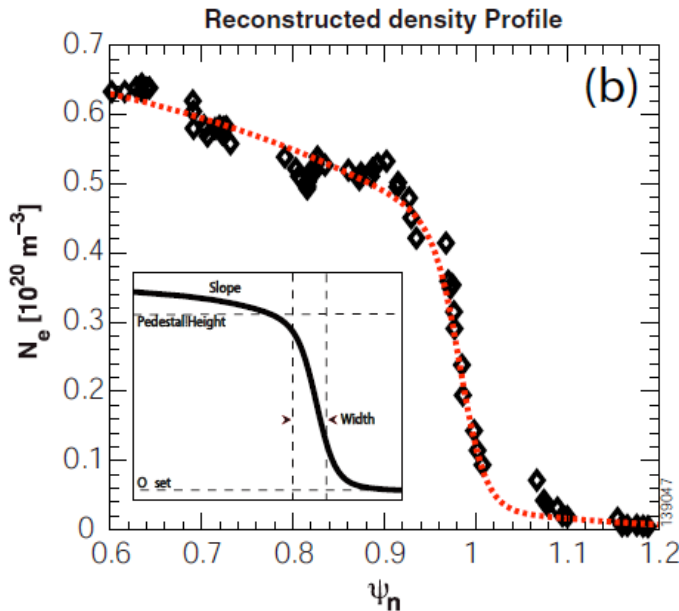The presence of strong gradients in the pedestal region is often correlated with rapidly growing instabilities known as edge localized modes (ELMs) in many toroidal confinement devices. These ELMs result in a periodic, substantial drop of the plasma stored energy (typically < 10%) on the timescale of several hundred μsec[2]. The reduction or elimination[3] of ELMs while maintaining high energy confinement is essential for the ITER, which has been designed for H-mode operation.

Detailed analysis has shown that large ELMs are triggered by exceeding either edge current density limits (kink/peeling modes) and/or edge pressure gradient limits (ballooning modes)[4-6]. Similar edge stability calculations using model equilibria have indicated that

Figure N1: example of reconstructed n_e profile, using multiple time slices and conditional averaging, in synchronization with the ELM cycle [Diallo, NF 2011].

spherical tokamaks should have access to higher pressure gradients and H-mode pedestal heights than higher aspect ratio tokamaks, owing to high magnetic shear and possible access to second stability regimes[7]. Generally speaking though, spherical tokamaks have observed a wide variety of ELM types, many in common with higher aspect ratio tokamaks[8, 9]; true ELM-free regimes with high pedestal pressure gradients have been rare. The use of lithium in NSTX has enabled access to such a high pedestal pressure regime, one in which the core stability limits with high normalized beta are observed with no sign of ELMs[10]; these will be discussed in the next section.

To project forward ELMy H-mode operating scenarios to NSTX Upgrade, low aspect ratio designs for a Fusion Nuclear Science Facility, and ITER, a series of experiments was conducted[11] in NSTX. The main goal was to experimentally measure the scaling of the H-mode pedestal structure, i.e. heights, widths, and
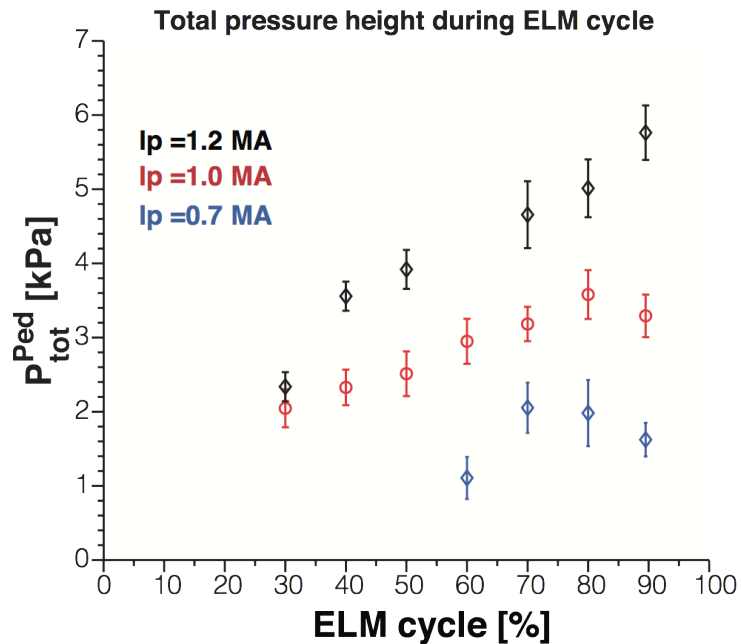

Figure N2: dependence of total pressure at the top of the pedestal as a function of the fraction of the ELM cycle, for 3 different values of I_p. [Diallo, NF 2011]
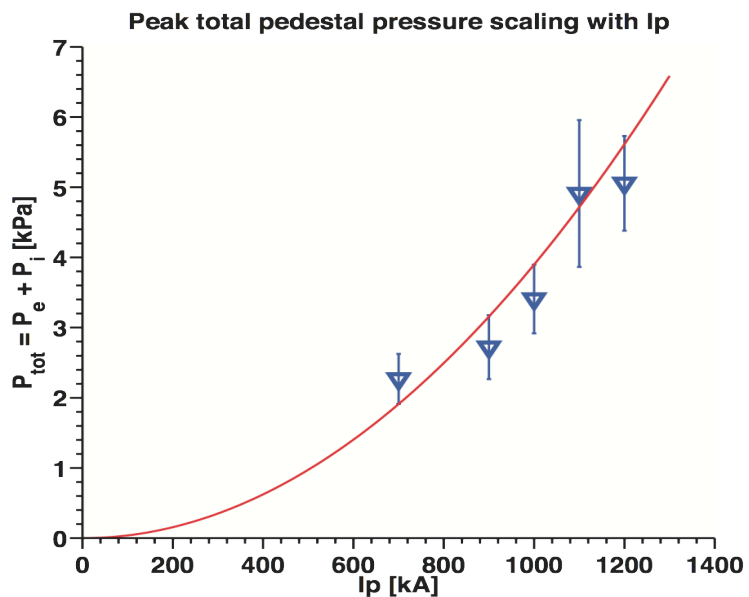

Figure N3: dependence of total pressure at the top of the pedestal as a function of I_p. [Diallo, NF 2011]

gradients, as a function of engineering parameters, e.g. plasma current I_p, toroidal field B_t, and lower divertor shape triangularity, δ_l. To the extent possible, we also attempted to compare results with available theoretical and numerical simulations. As described in the next section, we evaluated our edge stability with the PEST and ELITE codes, and interpreted our edge and divertor profiles and transport with the SOLPS code. While our original intent was to compare the pedestal structure measurements in this section with the EPED model[12], it was felt that the version of EPED under present development, EPED2, with a more accurate calculation of diamagnetic stabilization, would be more appropriate for future comparisons.

The experiments described in this section[11] were performed using neutral beam injected power from 4 to 6 MW. The discharges studied used a marginally double-null divertor configuration, with the plasma slightly biased downward, and the lower triangularity $\delta_l \sim 0.6$. The upper triangularity was typically kept at 0.4 and the elongation was kept between 2.3 and 2.4. To target ELMy discharges for studies reported here, a total of 50 mg of lithium was deposited on the bottom divertor plates between discharges. The key diagnostics utilized to characterize the pedestal parameters were the mid-plane Thomson scattering system[13] for electron density n_e and temperature T_e sampled at 60 Hz, the fully stripped C6+ charge-exchange recombination spectroscopy[14] for providing the carbon density and ion temperature T_i with a 10ms time resolution, and the divertor recycling light levels, e.g. D_α emission, for identifying ELMs. We characterized the evolution of the radial profiles between ELMs by reconstructing composite profiles synchronously with multiple ELMs. For this study, we focused on large type I ELMs of typical frequency ranging between 20 and 70 Hz. Individual radial profiles of density, temperature and pressure were first mapped using reconstructed EFIT equilibria[15, 16] in normalized poloidal flux coordinates ψ_n ($\psi_n = (\psi_c - \psi)/(\psi_c - \psi_{sep})$, where ψ_c and ψ_{sep} represent the poloidal flux at the core and at the separatrix, respectively). These individual profiles were then collated together as a function of their timing relative to the ELM cycle; this can be regarded as a correlated sampling approach. The electron profiles were fitted with 'standard' modified hyperbolic tangent fits, and the ion profiles were fitted with cubic splines. The resulting fit yields an estimate of the pedestal width (Δ) from which a gradient can be determined. The error in the fit in combination with an estimate of the scatter around the fit yields estimates on the error of the pedestal

parameters. An example of a reconstructed density profile using this technique is shown in Figure N1.

To capture details of the inter-ELM dynamics, the profile fits were performed around sliding temporal windows of 20% width. For example, we represent a window between 30% and 50% of an ELM cycle by its midpoint, which in this case is 40%. With this nomenclature, n_e or T_e *prior to* and *after* an ELM crash are identified as 90% and 30% of an ELM cycle, respectively.

As shown in Figure N2, we observed a clear buildup of the pedestal pressure before the onset of ELMs at all I_p, similar to observations in MAST[17] and AUG[18]. In the low and medium I_p cases, we observed a saturation of the pedestal height late in the ELM cycle, in contrast to the high I_p case where the pedestal height increased until ELM onset. A factor of 3 increase in pedestal height during the ELM cycle was observed at high I_p; this is similar to the 400% increase observed[19] in DIII-D. The saturation late in the ELM cycle in our data, however, contrasts with the DIII-D observations where the
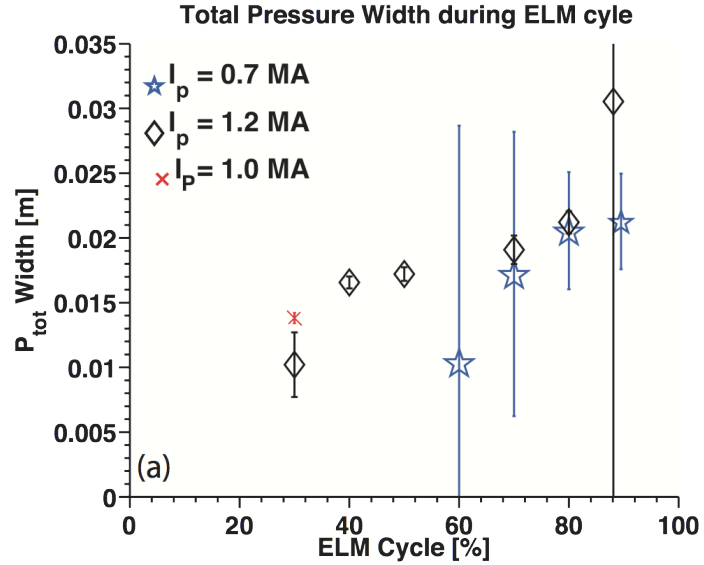

Figure N4: dependence of total pressure profile width as a function of the ELM cycle for three different values of I_p. [Diallo, NF 2011]
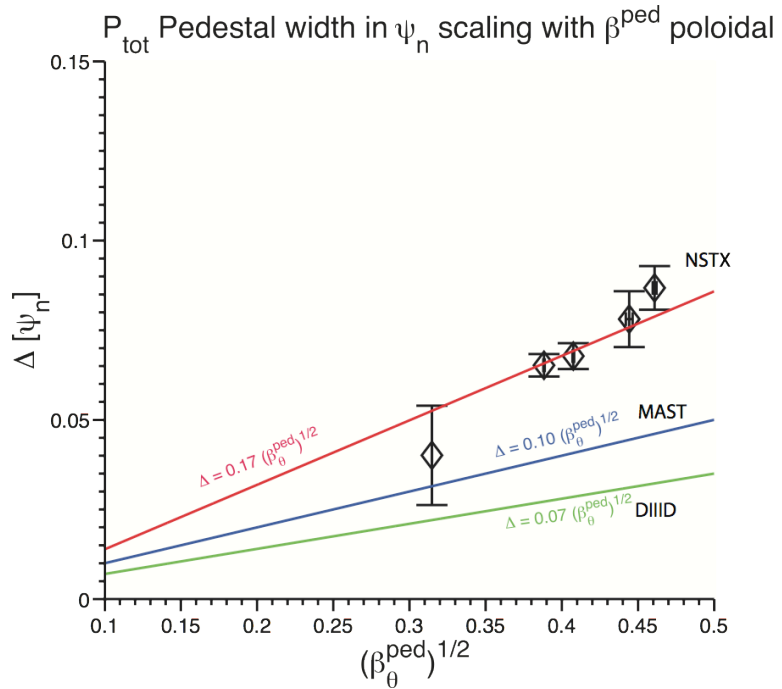

Figure N5: dependence of total pressure profile width as a function of normalized pedestal top pressure, β_θ^{ped}. [Diallo, NF 2011]

electron pedestal pressure saturates in the early phase, e.g. 20–50% of the ELM cycle.

It's clear from Figure N2 that the pedestal pressure increased with I_p. We display the total pedestal pressure during the last 20% of an ELM cycle as a function of I_p in Figure N3. There is a near quadratic increase in the pedestal height prior to the ELM onset (e.g. 90% ELM cycle) with I_p. Note that the B_t was 10% higher for $I_p = 900$ kA and 1.1MA than that of $I_p = [1.2, 1.0, 0.7]$ MA, but we show later that the pedestal parameters appear to be independent of B_t.

As shown in Figure N4, the pedestal width Δ increases until the onset of an ELM to a nominal value of ~2 cm (0.085 in ψ_n units), at both low and high I_p. Moreover the physical space width seems to be largely independent of I_p at comparable fractions of the ELM cycle. For the medium I_p case, only one point is included in the early stage of the ELM cycle as the remaining points have error bars too large to allow for meaningful comparison.
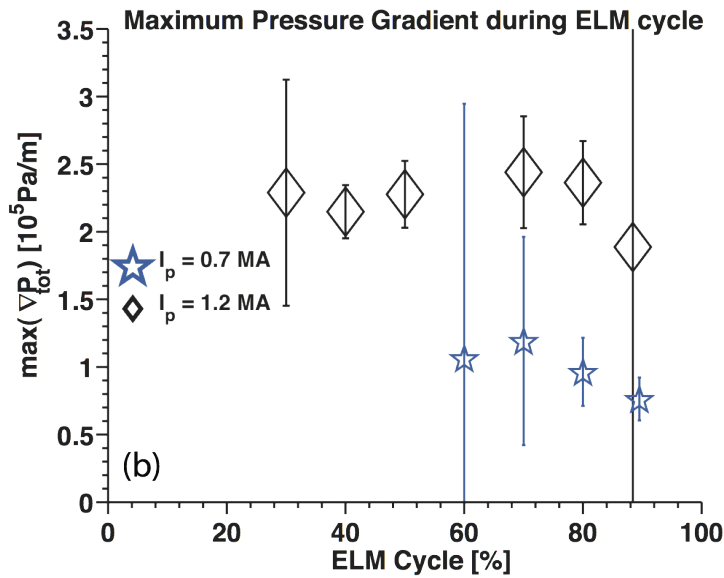

Figure N6: dependence peak pressure gradient in the H-mode pedestal as a function of the ELM cycle for three different values of I_p. [Diallo, NF 2011]

In contrast, Figure N5 shows a clear dependence of the pedestal width in ψ_n space prior to the type I ELM onset, e.g. the last 20% of an ELM cycle, with the square root of pedestal β normalized to the poloidal magnetic field, β_θ^{ped}. The approximately square root dependence is consistent with experimental observations in DIIID and MAST, except the fitted constant coefficient in NSTX is ~ 70% larger than that of MAST[20] and 2.4 times greater than that of DIII-D[21]. The reason for the difference in

Finally, Figure N6 shows the maximum pressure gradient for various parts of the ELM cycle. While there is clearly an increase in the maximum pressure gradient with I_p, the maximum pressure gradient remains constant during the ELM cycle. This lack of variation in the maximum pressure gradient is consistent with recent observations in both AUG[22] and DIIID[19, 23], where the maximum pressure gradient initially increases and is limited at an early phase of the ELM cycle. In our case, the increase in the pressure prior

to its saturation (before the 20% of the ELM cycle) could not be resolved. Hence, in view of this saturation prior to the ELM crash, the pressure gradient appears to play a weak role in the triggering of an ELM. In the framework the peeling–ballooning physics, it is plausible that the edge current could play the key role just prior to the ELM crash.

Finally we measured the dependence of the pedestal pressure height on lower divertor triangulariy, δ_l, and B_t. Figure N7 shows that the pedestal height increased with δ_l, although there is substantial scatter at any given δ_l. Initial measurements of the effects of B_t on pedestal height showed a negligible correlation. These data were obtained over a small range of B_t in ELMy discharges and a larger B_t range in ELM-free discharges, as shown in Figure N8. Future experiments in NSTX Upgrade are needed for more confidence in these two dependences.
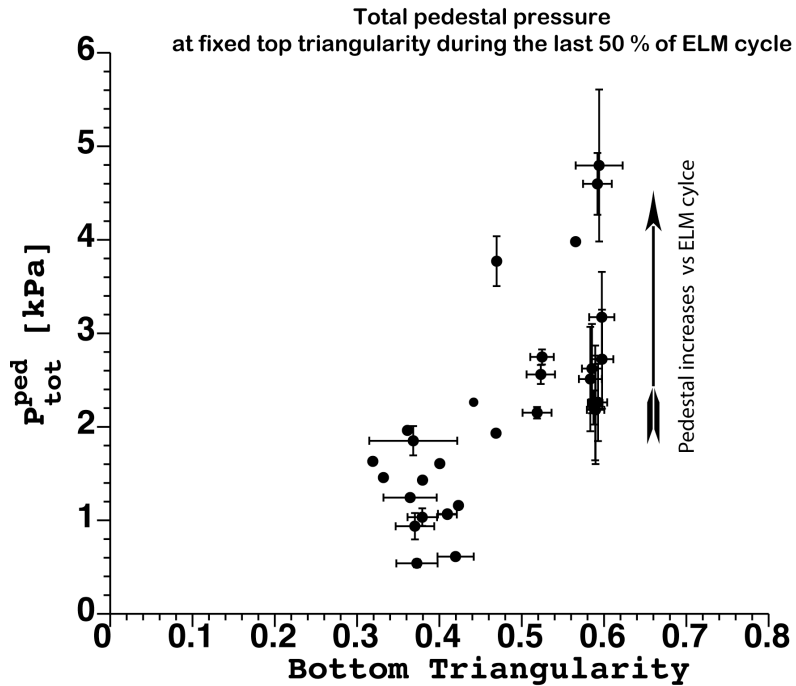

Figure N7: dependence of total pressure at the top of the pedestal as a function of lower divertor triangularity, δ_l during the last 50 % of the ELM cycle. The arrow indicates the increase of the pedestal height at fixed top and bottom triangularities. [Diallo, NF 2011]
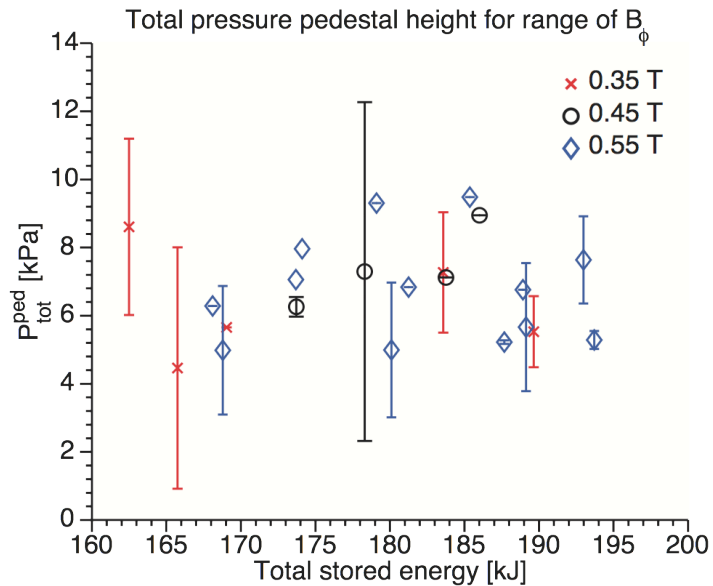

Figure N8: dependence of total pressure at the top of the pedestal as a function of B_t. This dataset was taken in ELM-free discharges, but the trend is reflected in the ELMy discharges, albeit in a narrower range. [Diallo, NF 2011]

9

FES Joint Facilities Research Milestone 2011 – NSTX final report

The density fluctuations at various stages of an ELM cycle were obtained using the 16-channel reflectometer probing the edge plasma; the analysis procedure was described elsewhere[11]. The observed density fluctuations exhibit a coherent peak in the vicinity of 12 kHz at the top edge of the density pedestal. The overall fluctuation level decreases prior to the onset of ELM. The characteristics of the 12 kHz coherent fluctuation observed in the density fluctuations could not be attributed to modes detected on Mirnov signals, which indicates that either the peak density fluctuation spectra are too weak to be detected by Mirnovs or that they are electrostatic. Nonetheless, the observed fluctuations suggest that they are not likely to play a role in constraining the profiles inside the edge barrier, and they clearly do not exhibit the characteristics of kinetic ballooning modes, which are postulated to set the pedestal width in the EPED model[12].

FES Joint Facilities Research Milestone 2011 – NSTX final report

II. ELMy to ELM-free transition with lithium wall coatings

Lithium wall coatings have been used in a variety of devices to control edge recycling and improve energy confinement[24-28], and their use is a focal point of experiments in NSTX. Hence, analysis of the effect of lithium on edge plasma characteristics represents one of the unique contributions form NSTX toward this Joint Research Target report. Most of the data discussed in this section was obtained in previous years, but the in-depth analysis reported here was conducted in FY 2011.

Lithium was first introduced into the National Spherical Torus Experiment (NSTX) in 2005 via pellet injection, with modest, short-lived effects on the discharge characteristics[29]. A lithium evaporator (LiTER) was installed in 2007 to coat the lower portion of NSTX, resulting in reduced recycling, improved energy confinement, and a reduction of edge instabilities known as ELMs[30]. In 2008, a second LiTER was installed into NSTX to provide 360^0 coverage of the lower divertor, thereby eliminating shadowed regions[31, 32]. Lithium from the previous campaign's experiments had been removed by sanding of the tiles during the vent prior to the operations. Approximately a month of dedicated experiments using periodic boronization of the graphite plasma-facing components (PFCs) was used to provide reproducible ELMy H-modes with good energy confinement.

A reference scenario with ordinary Type I ELMs was developed several years ago in an Alcator C-Mod/MAST/NSTX similarity experiment[33] on small ELM regimes. These ELMs had a fractional stored energy drop $\Delta W/W \sim$ 2-5%, nominal frequency of ~ 100 Hz that increased with heating power, in a boundary shape with a relatively high X-point for NSTX, with $\delta_r^{sep} \sim$ -5mm. Here δ_r^{sep} is the distance between the two X-points mapped to the outer midplane, where the convention that $\delta_r^{sep} < 0$ means the lower X-point is closer to the plasma than the upper X-point. There are no small, Type V ELMs in this discharge scenario, which are otherwise common[34] in NSTX. Other relevant discharge parameters were: I_p=0.8 MA B_t=0.45 T, P_{NBI}=4 MW, and line average electron density n_e from 4 - 6.5 x 10^{19} m^{-3}. Periodic boronizations in the run campaign had been applied prior to this experiment.

The lithium was then introduced gradually but systematically, to thoroughly document its impact on global discharge characteristics, including ELM activity, as well as plasma profiles. The amount of lithium deposition between discharges was chosen

carefully such that the transition from ELMy to ELM-free discharges would occur over at least 10 discharges. HeGDC of 6.5 minute duration was used between all of the discharges, followed by lithium evaporation from two overhead evaporators. Note that subsequent experiments demonstrated that HeGDC is unnecessary with lithium coatings between discharges. During the plasma discharges, a shutter was used to prevent lithium evaporation into the vacuum vessel to avoid coating of the windows. Additional details of this experiment and preliminary analysis are published elsewhere.[35]

Figure N9 shows the lithium deposition between discharges during the sequence, as well as the cumulative deposition. The deposition rate was kept approximately constant between the first 9 discharges starting with #129021, and was gradually increased afterwards. We emphasize that this sequence was the first use of lithium in this campaign, insuring that the reference discharges were truly pre-lithium. The gas fueling, P_{NBI}, and boundary shape were held constant until the very end of the scan, when higher fueling and

Figure N9: Amount of lithium deposition before subsequent discharge, and cumulative deposition in the discharge sequence. [Boyle, PPCF 2011]

lower P_{NBI} were needed to avoid low density locked modes and resistive wall modes.

The evolution of the divertor D_α for the sequence is shown in Figure N10. The external gas fueling was held constant until #129036, and then it was increased or the subsequent discharges. The P_{NBI} was held constant at 4 MW until #129033, after which it was reduced in steps to avoid the locked modes.
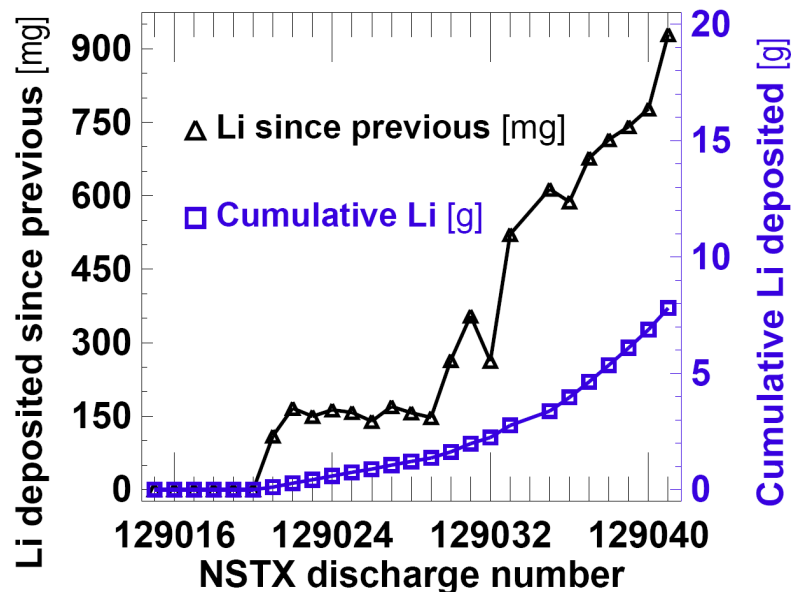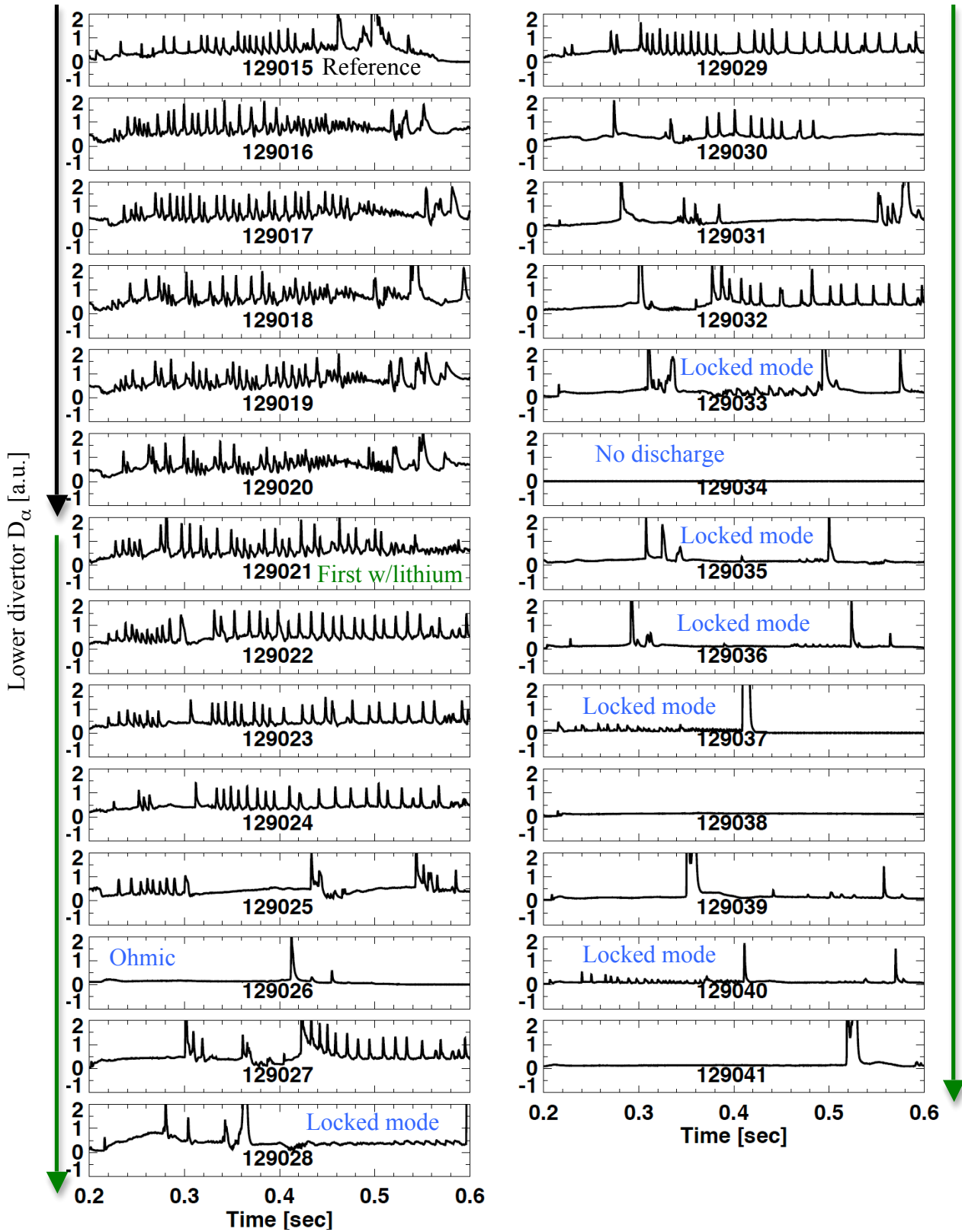
Figure N10: Evolution of lower divertor D_α emission during discharge sequence, showing the gradual effect on ELMs. The black vertical arrow indicates reference, non-lithiated discharges, and the green arrows show lithiated discharges.

FES Joint Facilities Research Milestone 2011 – NSTX final report

The effects of lithium are apparent in the second lithiated discharge #129022, in that the ELM frequency was reduced. ELM-free periods of increasing duration are evident after #129024, but the progression to full ELM-free operation was not monotonic. Even as more lithium was added, fully ELMy discharges returned (129027, 129029, 129032). These ELMy discharges all coincided with a sustained period of low confinement, high recycling L-mode at the end of the previous discharge (129026 had no neutral beam heating; 129028 and 129031 suffered locked modes). Discharges 129029 and 129030 also suffered locked modes and ended in periods of L-mode but were followed by discharges with ELM-free phases. However, these L-mode periods were shorter and had very low stored energy. One possible explanation[36] for the return of ELMs is that the accumulated lithium was passivated by the sustained L-mode discharges, and the amount of fresh lithium in these discharges was by itself insufficient to suppress ELMs. Discharges 129033, 129036, 129038 and 129041 were ELM free despite following periods of sustained and/or high stored energy L-mode. In these cases, the thick coatings of fresh lithium were able to suppress ELMs by themselves, regardless of the condition of the previously accumulated lithium.

The discharges #129033 and #129035 - #129037 did not achieved sustained H-mode phases, as the combination of heating power (P_{NBI}=2 MW) and external fueling was not optimized until #129038. Discharges #129039 and #129041 both disrupted at 0.35sec and 0.515 sec respectively, as a result of higher β_N from an increased of P_{NBI} to 3 MW. In addition, #129041 had modestly higher external gas fueling than #129038 and #129039.

The evolution of other relevant plasma parameters during the scan is shown in Figure N11. Panel (a) shows that the lower divertor D_α at t=0.4 sec gradually decreased with increasing lithium coatings, dropping substantially at the highest coating values. The upper divertor D_α at t=0.4 sec gradually decreased with increasing lithium coatings also (panel (b)), showing an even larger fractional drop than the lower divertor D_α; this suggests that the lithium evaporated into the lower divertor might have been transported to the upper divertor through plasma-wall interactions, where it reduced recycling. The line-average density at t=0.4 sec was gradually reduced also, while the peak plasma stored energy W_{MHD} and β_N (generally between 0.45 and 0.6 sec) from equilibrium reconstructions[16] gradually increased. Again, the last three discharges had reduced P_{NBI}

compared to the other discharges. Finally panel (f) shows that the confinement enhancement factor relative to the ITER97-L scaling increased slowly during the coating scan.

The electron kinetic profiles were correlated with the amount of pre-discharge lithium deposition, as shown in Figure N12. The n_e peaking factor initially increases as the lithium deposition is increased; this is due to a general reduction in the edge density. As the discharges became less ELMy, the density profile gradient was reduced, leading to a reduced peaking factor in the latter half of the discharge sequence. On the other hand, the T_e and P_e profiles peaking factors decreased nearly monotonically with increasing lithium deposition, consistent with a analysis of a broader dataset[31]. The ion profile peaking factors did not show a clear trend during the scan.

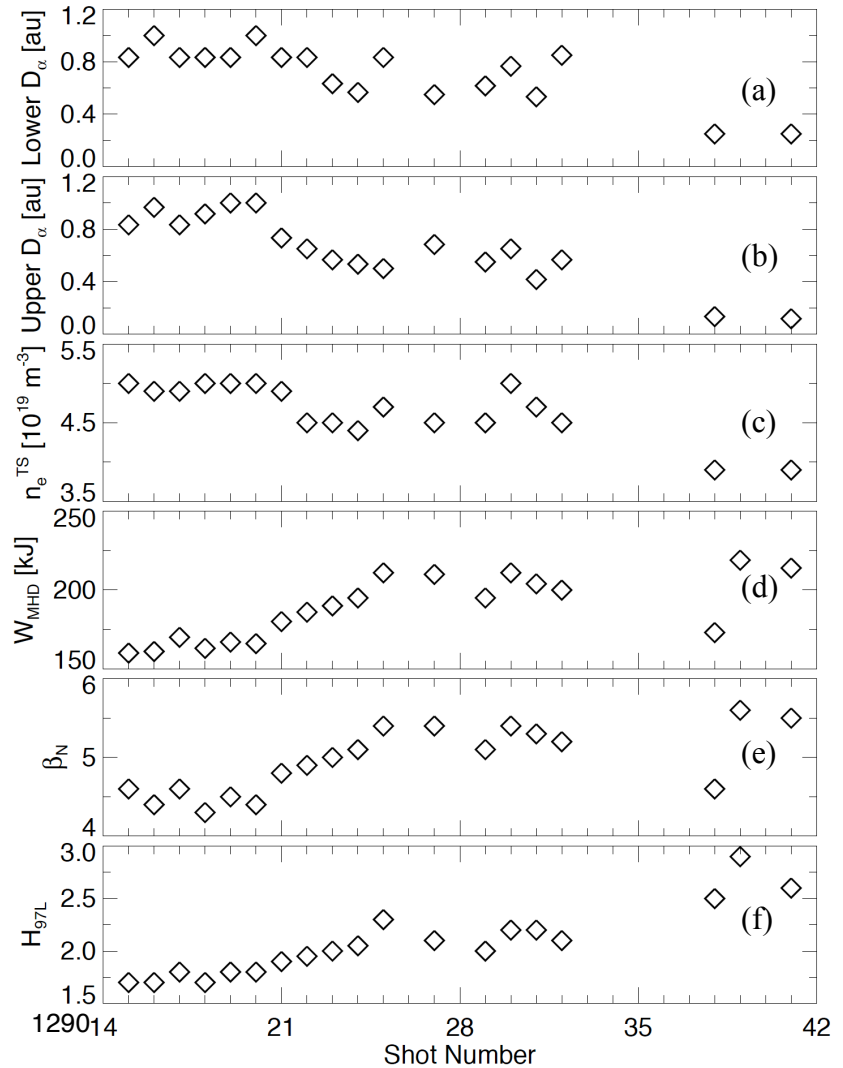The core transport during this scan was

Figure N11: Evolution of plasma parameters during systematic scan: (a) Lower divertor D_α baseline value at t=0.4 sec, (b) upper divertor D_α baseline value at t=0.4 sec, (c) line average density from Thomson scattering at t=0.4 sec, (d) peak stored energy W_{MHD}, (e) β_N at time of peak W_{MHD}, and (f) energy confinement relative to ITER97-L scaling at time of peak W_{MHD}. Lithium was added starting with #129021. The P_{NBI} and gas fueling were varied in the final three discharges. [Maingi, PRL 2011]

evaluated with the TRANSP code[37, 38]. The procedure uses the kinetic n_e and T_e profiles from Thomson scattering data, the T_i and n_C data from CHERs, Z_{eff} from visible Bremsstrahlung radiation, radiated power from bolometry, reconstructed equilibrium from the EFIT code[15, 16], and neutral beam (NB) data. Monte Carlo techniques are used to compute the NB deposition, and no fast ion diffusion was used. A match to the neutron rate was achieved by varying the edge neutral density. The analysis showed[39] that both the total and electron τ_E increased with increasing lithium deposition; indeed, the electron τ_E increased more rapidly than the global τ_E. In addition the edge electron thermal diffusivity at r/a=0.7 χ_e decreased strongly with increasing lithium deposition; in contrast the ion thermal diffusivity χ_i actually increased modestly. On the other hand, the core χ_e, χ_i, and χ_ϕ at r/a=0.35 were insensitive to or weakly increasing with the pre-discharge lithium deposition. These results agree with analysis[40] of a broader dataset, which included a few of the discharges from this scan.

To illustrate the dramatic effect of high lithium deposition between discharges (> 400 mg), we now compare the time evolutions for a reference ELMy discharge with two completely ELM-free discharges. Figure N13 shows the evolution of a
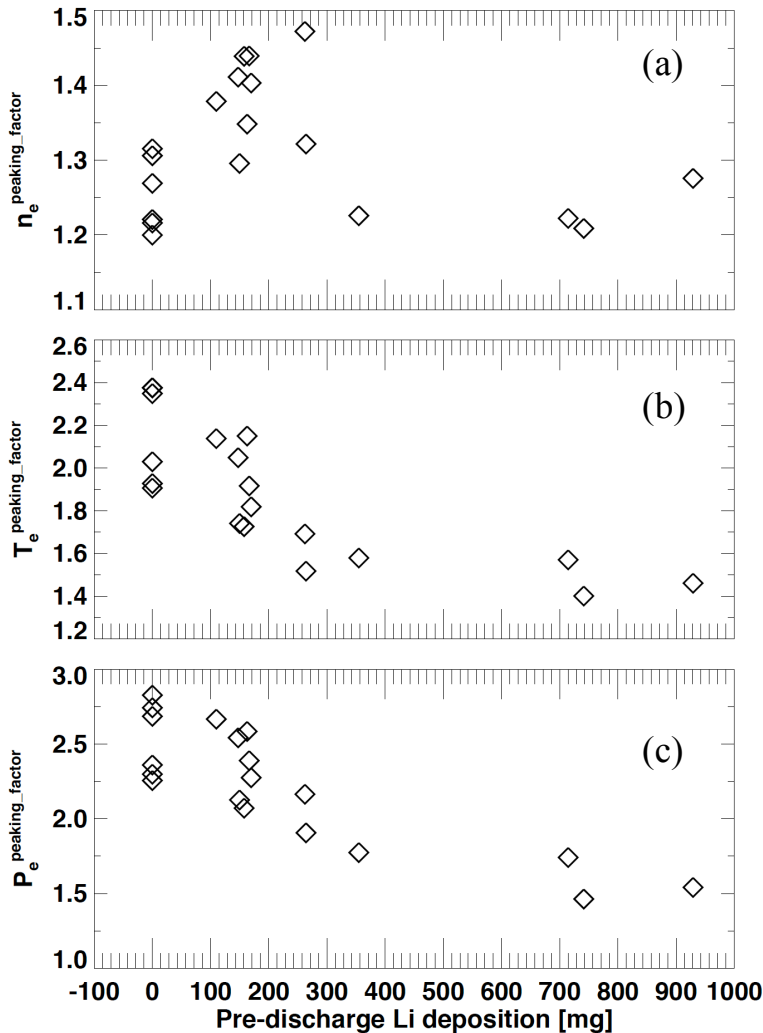

Figure N12: Dependence of profile peaking on lithium deposition: (a) n_e profile peaking factor, (b) T_e profile peaking factor, and (c) P_e profile peaking factor. [Maingi, PRL 2011]

boronized ELMy discharge (black), with two lithiated discharges, one with low input power (orange), and one with intermediate input power (blue). Panel (a) shows that the ELM-free discharges lasted longer, and panel (b) shows the ELM activity as spikes on the divertor D_α emission. Note that the baseline divertor D_α emission was substantially lower in the with-lithium discharges, indicating reduced recycling. At these high inter-discharge evaporations, the energy confinement τ_E increased such that the heating power needed to be reduced to avoid the global stability limit[10, 35]; hence, panel (c) shows a range in P_{NBI} from 2 to 3 MW in the discharges with lithium, compared with P_{NBI}=4 MW in the reference discharge. Note that the discharges with lithium near the end of the lithium coating scan with P_{NBI}=4 MW had large locked modes shortly after the I_p flat-top (not shown). Panel (d) compares the normalized plasma pressure β_N, where $\beta_N=\beta_t B_t a_m/I_p$, and $\beta_t=4\mu_0 W_{MHD}/(3V_p|B_t|^2)$ is the plasma pressure normalized to the on-axis vacuum toroidal field B_t, a_m is the minor radius, I_p is the plasma current, μ_0 is the permeability of free space, and W_{MHD} and V_p are the plasma stored energy and volume from equilibrium reconstructions. Despite the reduction in P_{NBI} from 4 to 2 MW, the orange and black discharges had nearly identical peak β_N and stored energy. An additional 1 MW of NBI power in the blue discharge increased $\beta_N \sim 5.5$, i.e. where resistive wall modes are typically encountered[41, 42] in NSTX. Indeed the sudden drop in β_N in the blue discharge at ~ 0.5 sec was correlated with magnetohyrodynamic (MHD) activity typical of resistive wall modes. Panel (e) shows that the τ_E normalized by the ITER-97 L-mode global scaling[43] was 50% higher in the with-lithium discharges. The discharges with lithium in Figure N13 showed reduced early density and dN/dt, although the eventual density in the lowest power discharge reached the same value as the reference discharge, partly because of the lack of ELMs. Also the radiated power fraction increased with time in these ELM-free discharges[10, 30, 31, 35], because ELMs typically flush impurities, preventing temporal accumulation. While this temporal increase in radiated power is a hindrance in developing these lithiated ELM-free discharges into long pulse scenarios, other methods have been shown to reduce impurity accumulation, e.g. with pulsed 3-D fields[44, 45] or use of the "snowflake divertor" configuration[46].

The effect of lithium conditioning on the plasma kinetic profiles for the 2 MW lithiated and 4 MW boronized discharges from Figure N13, is displayed in Figure N14.

17

FES Joint Facilities Research Milestone 2011 – NSTX final report

The technique used for the profile analysis is described elsewhere[47]; briefly, synchronization with the ELM cycle is used to produce conditionally-averaged profiles from a number of the ELMy reference discharges, while 100 ms windows are used to construct composite profiles in the ELM-free discharge, #129038 from Figure N13. Panel (a) shows that the electron density n_e gradient (from Thomson scattering[13, 48]) was clearly reduced in the lithiated discharge, while panel (b) shows that the edge ion temperature T_i from charge exchange recombination spectroscopy was markedly higher. Panel (c) shows that the electron temperature T_e gradient was comparable near the separatrix from
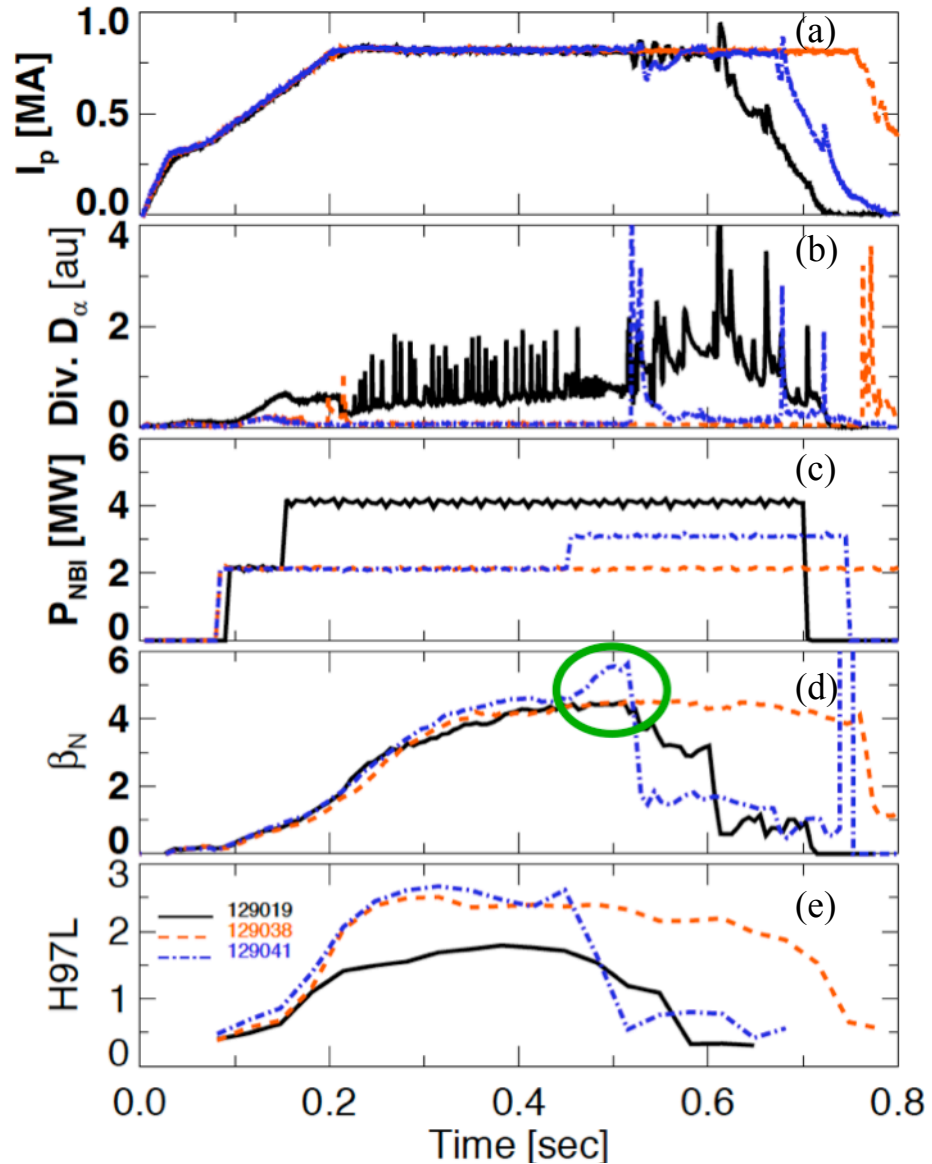

Figure N13: Comparison of one of the reference pre-lithium ELMy discharge (black), and two with-lithium discharges with different NBI power (blue, red): (a) plasma current I_p, (b) upper divertor D_α emission, (c) neutral beam injected power P_{NBI}, (d) normalized plasma pressure, β_N (e) confinement time relative to ITER97L scaling.

normalized poloidal flux ψ_N to 0.95-1.0, but the steep gradient region extended into ψ_N of 0.8 in the with-lithium discharge. Panel (d) shows that the edge ion toroidal rotation from CHERs was higher in the lithiated discharge, despite the reduction in neutral beam power/torque. Note that that the peak pressure P_{tot} and its gradient were shifted radially inward farther from the separatrix[10]. The changes to the ion pressure profile were subtle[36], because the increase in T_i was offset by a decrease in ion density, due to increased Z_{eff}. Hence the total pressure gradient was dominated by the electron gradients in all cases. Two ELM-free pressure profiles are shown in panels (e) and (f) to demonstrate that the peak pressure gradient was actually higher in some of the ELM-free composite profiles, but was generally shifted inward away from the separatrix, i.e. at ψ_N=1. This inward shift of the pressure profiles with lithium resulted in a similar shift of the bootstrap current, which was stabilizing to the kink/peeling modes thought to be responsible[10] for these ELMs in NSTX.

Fig. N15 shows that the measured ELM frequency during discharges from this sequence decreased with increasing discharge number, i.e. increasing lithium deposition. Clearly, the transition to ELM-free operation was not quite monotonic, however, in that several discharges with substantial ELM-free periods were followed by ELMy discharges. The data points in black had edge profiles that were
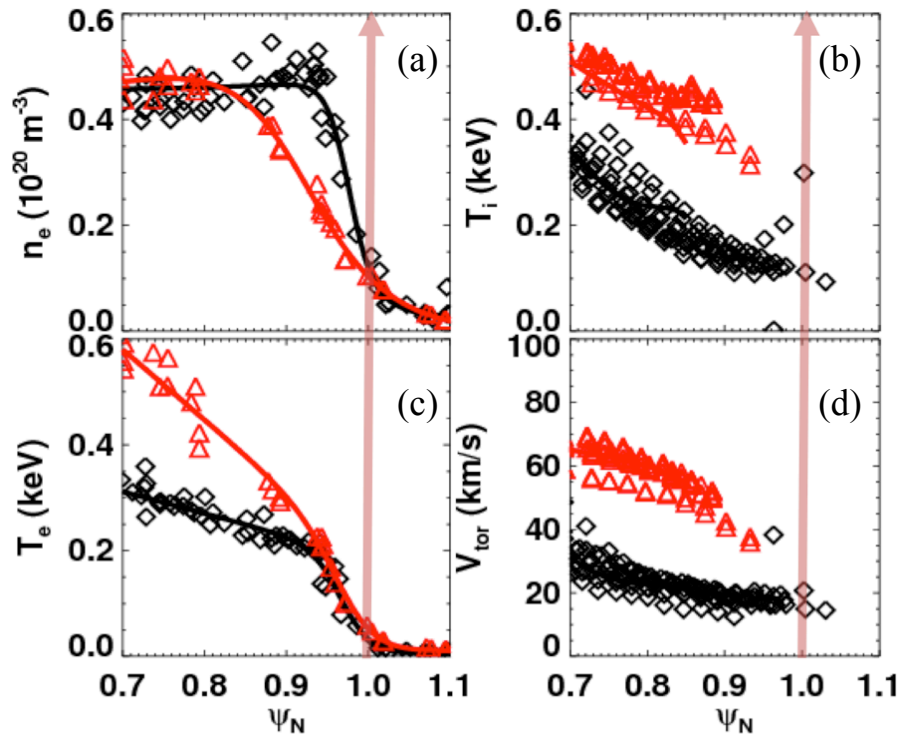

Figure N14: Profile comparison of no-lithium (black) and with-lithium discharges (red): (a) n_e, (b) T_i, (c) T_e, (d) V_{tor}, for pre- and with-lithium discharges.

analyzed with the ELM-synchronization method mentioned above, whereas the data points in blue were unsuitable for profile analysis, but were included for more insight into the trends. There are several discharges with more than one data point per discharge; in those cases, the edge profiles were analyzed in non-overlapping time windows of duration ~ 0.1 sec. This was necessary because the discharges had both an ELMy and an ELM-free phase, or long ELM-free phases with evolving density.

The n_e, T_e, and P_e composite profiles were fitted[36] with a 'standard' modified hyperbolic tangent ("mtanh") function[49], which includes both a tanh component and a linear component. The ELM frequency from the black data points is shown as a function of these pedestal widths in panels N15 (b), (c), and (d). The additional data points in red were obtained in discharges with heavy lithium wall coatings run in the 2009 campaign, using the same discharge programming and reduced P_{NBI}, as in #129038. The n_e and P_e profile widths are both shown to order the ELMy and ELM-free data, mostly as a threshold criterion. The T_e profile width can be immediately ruled out as an ordering parameter. Since the lithium mainly changes the recycling and the edge fueling, these trends support the hypothesis that the density profile change is central to the ELM suppression.

In addition to the profile widths, the mtanh profile fitting yields the pedestal top value and its location, the peak gradient and its location, and the pedestal bottom value and its location. A thorough analysis of the correlation between ELM frequency and the other parameters from the tanh fits showed that ELMy and ELM-free discharges were also organized by the location of the peak n_e and P_e gradients[36], i.e. the symmetry point of the tanh function. Panels N15(e) and (f) show the ELM frequency vs. distance of the n_e and P_e symmetry point from the separatrix; indeed, there is a threshold distance that organizes the ELMy and ELM-free data. This is unsurprising, because as the characteristic width of a profile grows, the location of its peak gradient shifts also, provided the location of the bottom of the profile remains fixed. It is relevant, however, because the location of the symmetry point coincides with the location of the peak bootstrap and local parallel current in the kinetic equilibria; increasing the separation between this current and the separatrix improves stability to kink/peeling modes. Note that the 2009 data are not included in panels N15(e) and (f) because of possible systematic uncertainty in the separatrix location for those discharges relative to the main sequence in Figure N9; this

uncertainty would affect the computed symmetry point to separatrix distance, but not the profile widths in panels N15(b), (c), and (d).

Many of the discharges in this sequence were simulated[50] with the 2-D edge plasma and neutrals code SOLPS[51], to interpret and quantify the change in edge recycling and transport. Parallel transport in SOLPS is classical, with kinetic free-streaming corrections. Recycling and other neutral source terms are computed with the Monte Carlo code, EIRENE[52]. Cross-field transport is anomalous and user-defined; in these simulations, radial profiles of the particle and thermal diffusivities were iterated to match the midplane n_e, T_e, T_i, and fully stripped carbon density profiles. Here the radial transport was independent of poloidal angle; other simulations have also been done with poloidally dependent transport[53]. Recycling and power balance were used to match the outer divertor D_α and heat flux.
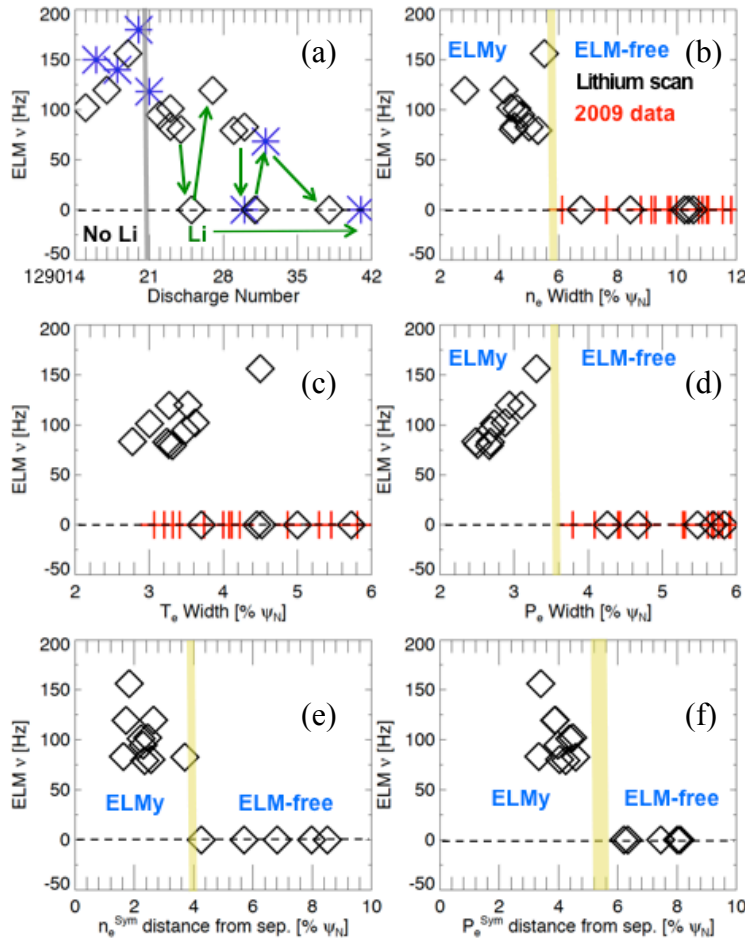

Figure N15: (a) Average ELM frequency during the scan; discharges with both ELMy and ELM-free periods of duration > 100ms are shown with multiple data points. (b) ELM frequency dependence on the fitted widths of the (b) n_e, (c) T_e, and (d) P_e profiles. Panels (e) and (f) show the ELM frequency vs. the distance from the n_e and P_e tanh function symmetry points from the separatrix. Converged tanhh fits could not be obtained for the blue data points in panel (a), but they are included to reflect the ELM frequency trend. Data from additional similar, more recent discharges are included in red in panels (b), (c), and (d), but additional uncertainty in the separatrix location precludes their addition in (e) and (f).

Thus, the final particle and thermal diffusivity profiles can be compared to interpret the effect of lithium on cross-field transport coefficients. No attempt was made to determine a particle or thermal pinch; hence, the diffusivities should be interpreted as 'effective' cross-field transport coefficients. The full procedure is described elsewhere[50, 54], and summarized below.

The peak value of the lower, outer divertor D_α profiles[55] was used to constrain the divertor recycling coefficient, R_p. The reference ELMy discharge peak D_α emission is matched using $R_p \sim 0.98$, while the ELM-free peak D_α emission was matched with $R_p \sim 0.90$. The trend is nearly identical to previous results[50] that did not model the impurities beyond a sensitivity assessment. In addition, these calculations matched the peak divertor heat flux from infrared thermography[56, 57], which effectively constrain the separatrix n_e and T_e values. The match to the available profile data for the reference ELMy discharge #129015 and the ELM-free discharge #129038 was quite good[50]. Both sets of simulations reproduce the data sufficiently well to assess the effect of lithium on the inferred effective radial transport rates.
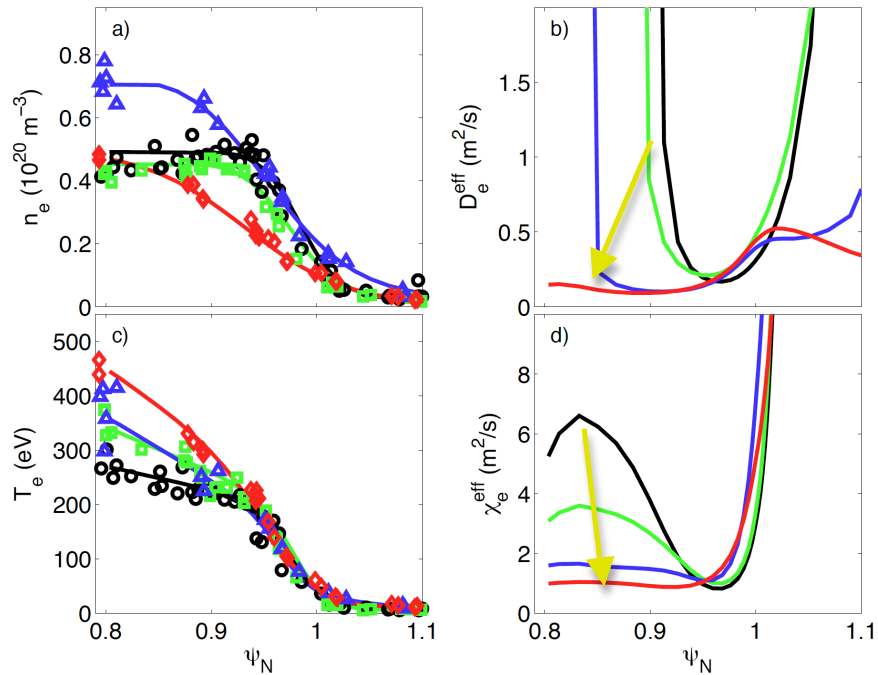

Figure N16: Modeling results for four discharges during the lithium deposition scan: (a) n_e, (b) T_e, (c) effective cross-field electron diffusion coefficient D_e^{eff}, and (d) effective cross-field electron thermal diffusivity, χ_e^{eff}. The yellow arrows indicate the trend with increasing lithium deposition. [Canik, PoP 2011]

Figure N16 shows the results of the 2-D modeling[54] for four of the discharges from the scan: a reference ELMy discharge based on composite ELM-synchronized plasma profiles (from #129015-019), an ELMy discharge near the transition to ELM-free operation (#129030), the subsequent ELM-free discharge (#129031), and the penultimate ELM-free discharge (#129038). Panel (a) shows the match to the n_e profiles, panel (b) shows the required effective particle diffusion coefficient, D_e^{eff}, panel (c) shows the match to the T_e profile, while panel (d) shows the corresponding effective electron thermal diffusivity, χ_e^{eff}. The simulations show that both the D_e^{eff} and χ_e^{eff} from the reference ELMy discharge had a minimum in the vicinity of the steep gradient region from $0.94 < \psi_N < 1$, indicative of the H-mode transport barrier. With increasing discharge number and lithium coatings, both the D_e^{eff} and χ_e^{eff} decreased gradually in the region from $0.8 < \psi_N < 0.94$, until the minimum transport level extended to $\psi_N = 0.8$, the inner domain of the calculation. The D_e^{eff} and χ_e^{eff} values actually increased modestly from $0.94 < \psi_N < 1$, and the D_e^{eff} dropped in the scrape-off layer, i.e. $\psi_N > 1$. The resilience of the T_e gradients from $0.94 < \psi_N < 1$ in panel (c) is notable, raising the prospect of transport regulation via electron temperature gradient (ETG) modes[54], as discussed below. In the next few paragraphs, we discuss the inferred changes to the edge turbulence from reflectometery, and evaluate both ETG modes and paleoclassical transport from the perspective of the observed transport changes with lithium.

NSTX is equipped with reflectometers[58] sensitive to n_e fluctuations in the pedestal region. The system used in these studies operates at five fixed frequencies (30, 35, 42, 44.5, 50 GHz), with quadrature detection used to separate the phase and amplitude of the reflected signals. These reflectometer frequencies allow density fluctuations to be probed from approximately the pedestal top ($n_e^{cutoff} \sim 3.1 \times 10^{19}$ at 50 GHz) to near the separatrix ($n_e^{cutoff} \sim 1.1 \times 10^{19}$ at 30 GHz). As is evident from the raw signals[54], the pre-lithium discharges show very strong amplitude fluctuations in the reflected signals due to scattering near the cutoff surface, whereas in the with-lithium discharges, this effect is much smaller and fluctuations are mainly in the phase. This alone implies a change in the turbulence characteristics, although the change in the n_e profile near the cutoff layer also needs to be taken into consideration. A quantitative estimate can be made for the change in the RMS density fluctuation level $\delta n/n$, using some assumptions about the

underlying turbulence and a synthetic diagnostic model. The inferred profiles of $\delta n/n$ in the pre-lithium and with-lithium discharges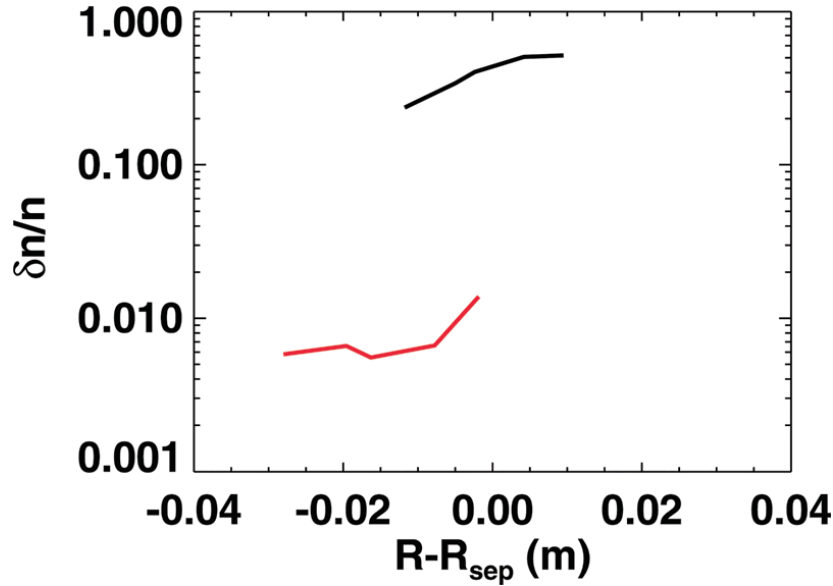 are shown in Figure N17. While this allows a comparison of the fluctuation level profiles between the pre- and with-lithium cases, in should be noted that the precise magnitude in the pre-lithium case remains somewhat uncertain given the assumptions required in making this estimate. Note that the innermost pre-lithium measurements are made in the inner part of the pedestal, near the top of the density pedestal, and these overlap with the outer channels for the with-lithium case. In this region of overlap, a reduction of density fluctuations from on the order of 10% pre-lithium to ~1% with lithium is inferred.

Figure N17: comparison of n_e fluctuation levels from reflectometry between pre-lithium (black) and with-lithium (red) discharges. [Canik, PoP 2011]

While the interpretive modeling and fluctuation measurements described above indicate that transport and turbulence are significantly reduced with lithium near the pedestal top, the underlying mechanisms for this reduction are under investigation. One candidate mechanism that can be considered is turbulence caused by ETG modes.

The critical gradient for ETG mode onset is given roughly[59] by

$$\left[\frac{R}{L_{T_e}}\right] = \max\left(\eta_e^{crit}\frac{R}{L_n}, \left(1+\frac{Z_{eff}T_e}{T_i}\right)\cdot\left(1.33+1.91\hat{s}/q\right)\cdot F_G\right)$$

where R is the major radius, L_{Te} and L_n are the temperature and density gradient scale lengths, $\eta_e = L_n/L_{Te}$, $\hat{s}$ is the magnetic shear, q is the safety factor, and F_G represents additional variations due to the MHD equilibrium that are not easily quantifiable for spherical torus parameters. The critical value η_e^{crit} is typically ~ 0.8 based on core ETG calculations, although a value of 1-1.25 was found[60] in the edge of ASDEX-Upgrade

plasmas. For both of the NSTX discharges[54], the n_e gradient is strong outside of $\psi_N \sim 0.95$, so that the ETG threshold can be expected to be set by the n_e gradient. The measured T_e gradient scale lengths are comparable to the n_e scale lengths in this region, suggesting that ETG may play a role in the fairly stiff T_e profiles observed near the separatrix. Near the pedestal top, the n_e gradients are weaker in both the pre- and with-lithium cases, making the critical T_e gradients more sensitive to Z_{eff}, T_e/T_i, and the q-profile. Based on this simple analysis, it does appear that ETG may be a contributor to the total transport at least in the with-lithium case, where only small low-k fluctuations are measured. Indeed, recent experiments where ELMs changed the edge density gradient, suppressed short wavelength ETG-like fluctuations, and reduced edge transport were recently reported[61].

Another possible mechanism for setting the edge transport rates is paleoclassical transport, which is driven by the diffusion of poloidal magnetic flux[62, 63]. Paleoclassical transport depends strongly on the neoclassical resistivity, and so is sensitive to the T_e and Z_{eff} profiles. Recently, a model of the pedestal structure based on paleoclassical transport within the pedestal and ETG transport at the pedestal top has been proposed, and predictions were made for the electron heat and particle transport rates[64].

Profiles of χ_e from the paleoclassical model are shown in Figure N18, along with the values from experiments, for the pre- and with-lithium cases[54]. Near the separatrix, the paleoclassical predictions reflect much of the structure seen in experiment, with χ_e being similar in magnitude and increasing with radius as ψ_N approaches 1.0. Furthermore, the paleoclassical values of χ_e also show the modest increase in the with-lithium case compared to pre-lithium observed near the separatrix. In the pedestal-top region, the experimental χ_e is significantly higher than the paleoclassical value for the pre-lithium case, suggesting that another transport mechanism dominates; in the with-lithium case, the agreement with paleoclassical remains good across the entire edge region.

The paleoclassical χ_e prediction[64] is proportional to the magnetic field diffusivity D_η induced by the parallel neoclassical resistivity. The neoclassical resistivity contains contributions from both the classical (Spitzer) resistivity (which depends on $Z_{eff}/T_e^{3/2}$), and parallel electron viscosity effects (which depend primarily on collisionality). In the steep gradient region ($0.94 < \psi_N < 1.0$) the density is reduced by $\sim 50\%$ in the with-lithium case. This reduces the collisionality and increases the viscosity effects by similar factors, and thereby increases the neoclassical resistivity (and χ_e) by $\sim 40\%$, as shown in Figure

N18. For $\psi_N<0.9$, the competing effects of larger Z_{eff} but higher T_e with lithium largely cancel and cause the pre- and with-lithium cases to have similar neoclassical resistivity, and hence χ_e magnitudes as seen in Figure N18.

The n_e profile can also be predicted using the paleoclassical model; note that a strong inward particle pinch is predicted that nearly balances outward diffusion, so it is more straightforward to compare the density profile directly rather than diffusivities. Figure N18 compares[54] the measured and predicted paleoclassical edge n_e profiles. The paleoclassical n_e profile is scaled so that the average edge density from the model matches the magnitude of the experimental data; note that the paleoclassical model predicts the profile shape only, and not the magnitude. Again, the paleoclassical model captures the experimental trends going from pre-lithium to with-lithium, with the n_e pedestal widening in the with-lithium case, with a reduced gradient within the pedestal. In this application of the paleoclassical model, the n_e profile shape is determined by the resistivity profile only; the particle source due to neutrals is neglected, since this is expected to play a small role in the model. We now move to discuss stability analysis of the discharge sequence.

Detailed stability analysis was performed for most of the discharges of this sequence[36] with the ELTE code[5, 6]. These calculations showed[36] that the ELMy discharges were all close to the current-driven kink/peeling mode boundary within our ability to reconstruct the profiles, while the ELM-free discharges were uniformly farther from their kink/peeling mode stability boundaries. To perform the stability analysis, free boundary equilibria were calculated using EFIT constrained by the fit pressure profiles, and by current profiles calculated using the Sauter neoclassical formula for the bootstrap current[65]. While the lack of an edge current measurement is a major source of uncertainty in the stability analysis, we note that the neoclassical value was found to be in agreement with lithium-beam measurements[66] on DIII-D. To map out the stability boundary, additional fixed boundary model equilibria were calculated with variations in the edge current and pressure gradient.

The stability criterion is commonly given by $\gamma_0/(\frac{1}{2}\,\omega_{*i})$, where γ_0 is the linear growth rate of the peeling-ballooning mode and ω_{*i} is the diamagnetic drift frequency. Contour plots of $\gamma_0/(\frac{1}{2}\,\omega_{*i})$ versus normalized edge current and normalized pressure gradient are shown in Figure N19 for four discharges selected for especially sharp

transitions in ELM behavior[36]. The crosshairs are centered on the experimental equilibrium and represent relative error in normalized edge current and normalized pressure gradient of 30% and 20%, respectively. The red region was unstable with $\gamma_0/(\frac{1}{2}$ $\omega_{*i}) > 0.15$; the blue region was stable with $\gamma_0/(\frac{1}{2}\ \omega_{*i}) < 0.05$. We note that $\gamma_0/(\frac{1}{2}\ \omega_{*i}) = 1$ marked the stability boundary to intermediate-n peeling-ballooning modes[47] in DIII-D, but the stability criterion has been found to be an order of magnitude lower for low-n kink/peeling modes[10, 67] in NSTX. In all of the discharges in this experiment, the equilibrium was closer to the current driven kink/peeling stability boundary, with the pressure driven ballooning boundary well off to the right hand side of the axis. In Fig. N19(a), a pre-lithium ELMy discharge was very close to the stability boundary. In Fig. N19(b) the stability boundary was much farther away for a discharge in which ELMs had been suppressed by intermediate
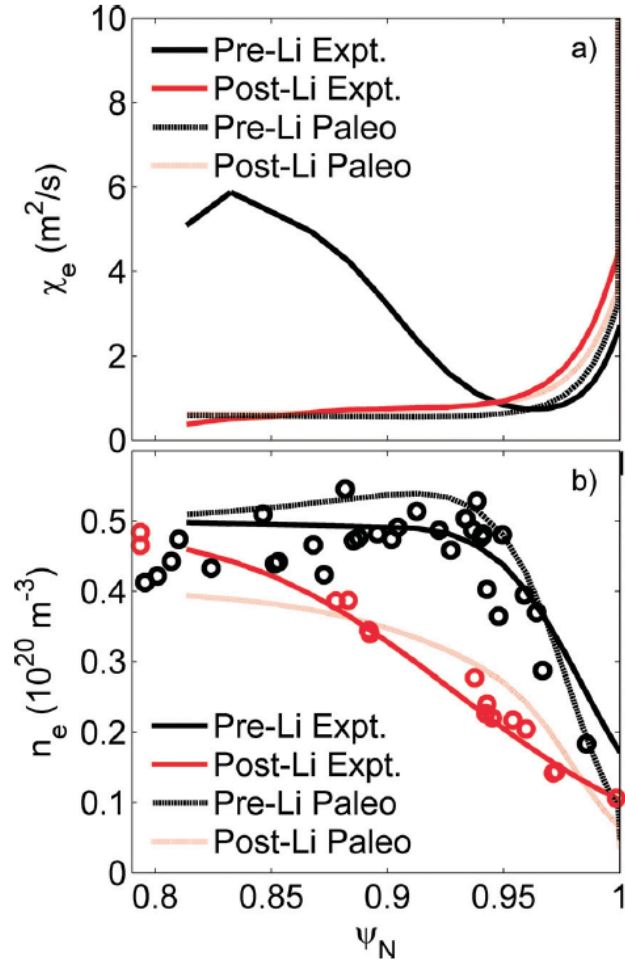

Figure N18: Experimental and paleoclassical values of a) χ_e^{eff} and b) n_e profile for pre-(black) and with-lithium (red) discharges. [Canik, PoP 2011]

lithium coatings. The improved stability was partly due to reduction of the edge current. More importantly, the stability boundary shifted to the left and upward; even with edge current comparable to the value in panel (a), this discharge would have been more stable. This shift in stability was probably because the pressure gradient and current peaks were shifted inward away from the separatrix. Fig. N19(c) shows a discharge in which ELMs returned, despite continued lithium deposition. Here, the stability boundary was very similar to the pre-lithium case, though the discharge had a significantly larger edge

current and pressure gradient. In the thick lithium coating, ELM-free discharge, [Fig. N19(d)], the edge current was about the same as the other ELM-free case, but the pressure gradient was lower, which in and of itself is destabilizing for kink/peeling modes. However, the stability boundary shifted to the left and up as the pressure gradient and current peaks shifted inward, making this discharge robustly stable. To summarize: the ELM-free equilibria were farther from their stability boundaries than the ELMy discharges. In the ELM-free discharges, the stability boundaries shifted to the left and up as the edge pressure gradient and current peaks widened and shifted away from the separatrix.

The above trend is clear at the endpoints[36]: other no-lithium discharges in this experiment were similar to Fig. N19(a), and thick lithium discharges from other NSTX experiments were similar to Fig. N19(d). Other intermediate lithium discharges in this experiment were more similar to Fig. N19(b) than Fig. N19(c). That is, their edge currents were ~20-40% below the stability boundary, whether or not they were ELMy. Given the number of steps involved in calculating the stability, it is unsurprising that it is difficult to resolve the precise transition from ELMy to ELM-free. However, it is clear that in general, ELM-free equilibria were farther from their stability boundaries than the ELMy discharges.

The reason for the enhanced stability is not simply a reduction in the peak pressure gradient; indeed, the peak pressure gradient was actually higher in some of the ELM-free discharges. The primary reason for the movement of the stability boundary is that the peak pressure gradient and calculated edge bootstrap current peak were shifted inboard farther from the separatrix, which is stabilizing for the peeling mode drive. Note that the low aspect ratio of the NSTX naturally results in the ballooning mode drive being insignificant for these ELMs.

To summarize, we have shown that many plasma parameters change nearly continuously with increasing lithium coatings in this section. Specifically, the divertor recycling was gradually reduced with increasing lithium wall coatings in NSTX, and the plasma stored energy and normalized τ_E all increased, while the core T_e and P_e profiles became less peaked with increasing lithium wall coatings. The inferred χ_e dropped sharply at r/a ~ 0.7. Interpretive 2-D simulations showed that the near-separatrix D_e^{eff} and χ_e^{eff} were reduced substantially from $0.8 < \psi_N < 0.94$, i.e. the H-mode pedestal

effectively expanded to the inner boundary of the calculation in the ELM-free discharge with lithium. The most dramatic changes to the profiles were in the pedestal region, where the n_e and P_e profile widths doubled. Interestingly, the edge T_e gradient remained approximately constant in the H-mode barrier region, but increased just inside the top of the pedestal with increasing wall coatings. The ion pressure profile was changed only modestly; hence, the total pressure profile reflected the modification of the electron pressure profile, whose peak gradient and associated bootstrap current moved farther from the separatrix. These profile changes were clearly correlated with the observed
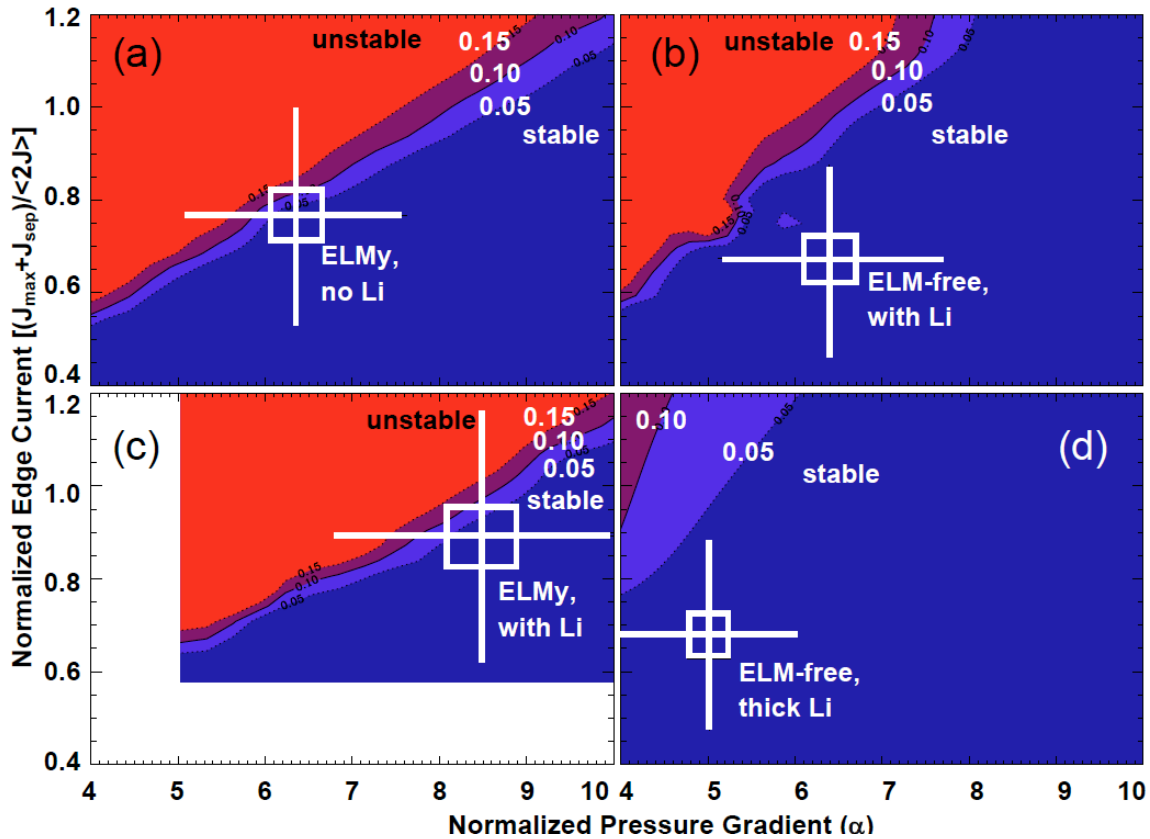

Figure N19: edge stability diagram for four discharges from the discharge sequence as computed with ELITE: ELM-free plasmas were farther from the kink/peeling stability boundary. Equilibria are from (a) a pre-lithium ELMy discharge, (b) an intermediate lithium discharge with reduced ELM activity , (c) an intermediate lithium discharge where ELMs have returned (no converged kinetic fits in blank space), and (d) a high lithium deposition, ELM-free discharge. Note that the axes have suppressed zeros. [Boyle, PPCF 2011]

gradual suppression of ELMs with increasing lithium, with reduced drive for the kink/peeling mode being the key stabilizing mechanism.

III. Enhanced Pedestal H-mode Characterization

The energy confinement multiplier relative to ITERH98y2 scaling, i.e. τ_E/τ_E^{H98y2}, typically obtained in spherical tokamaks with boron wall coatings is typically 0.8-1.0, albeit with different dependences than the international scaling[68]. The deployment of lithium wall coatings has helped[30, 40, 69] to increase τ_E/τ_E^{H98y2} up to 1.1-1.2*H98y2 in NSTX, but still short of the desired value for some future attractive STs designs. In general, improving the τ_E has merit for nearly all fusion concept designs, provided the
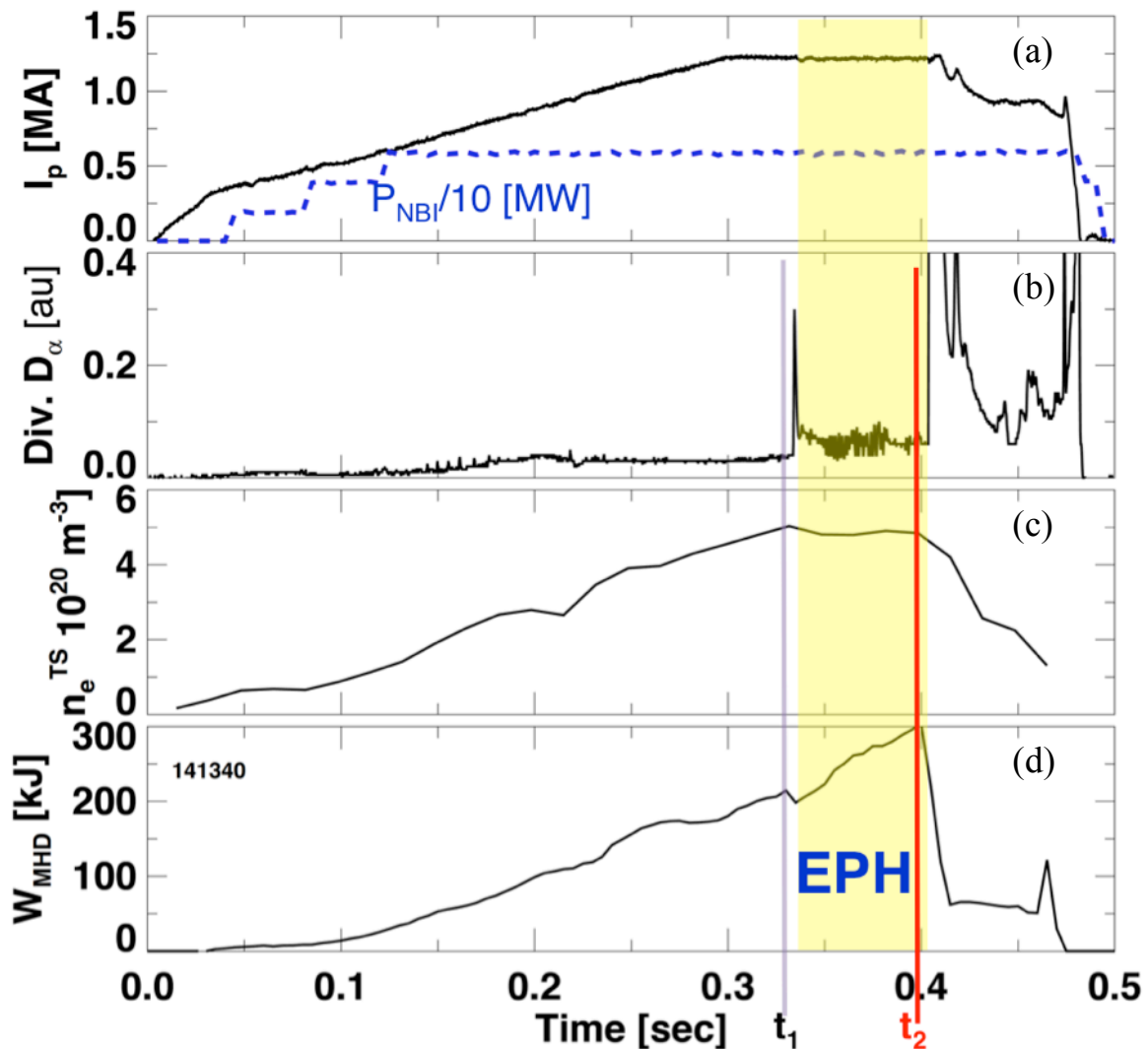

Figure N20:Evolution of a high I_p EP H-mode: (a) plasma current and NBI power (b) divertor D_α emission, (c) line-average density from Thomson scattering (d) and plasma stored energy. The EP H-mode phase is indicated in yellow.

scenarios do not introduce other problematic instabilities or excessive confinement of the helium ash and/or impurities.

Recently a spontaneous transition in H-mode discharges that results in a ~ 50% increase in τ_E was observed in NSTX. This increase is in addition to the 40-50% τ_E improvement provided by ELM-free lithium operation[10]. The improvement in τ_E is caused by a marked increase in the edge pedestal electron and ion temperatures (T_e, T_i), as well as a substantial broadening of the H-mode pedestal width, which has been referred to as the 'Enhanced Pedestal' (EP) H-mode[70, 71]. The electron density on the other hand, is observed to flatten. The EP H-mode is particularly interesting to study because of this apparent separation of particle and thermal transport channels.

The EP H-mode phase is triggered following certain large edge-localized modes
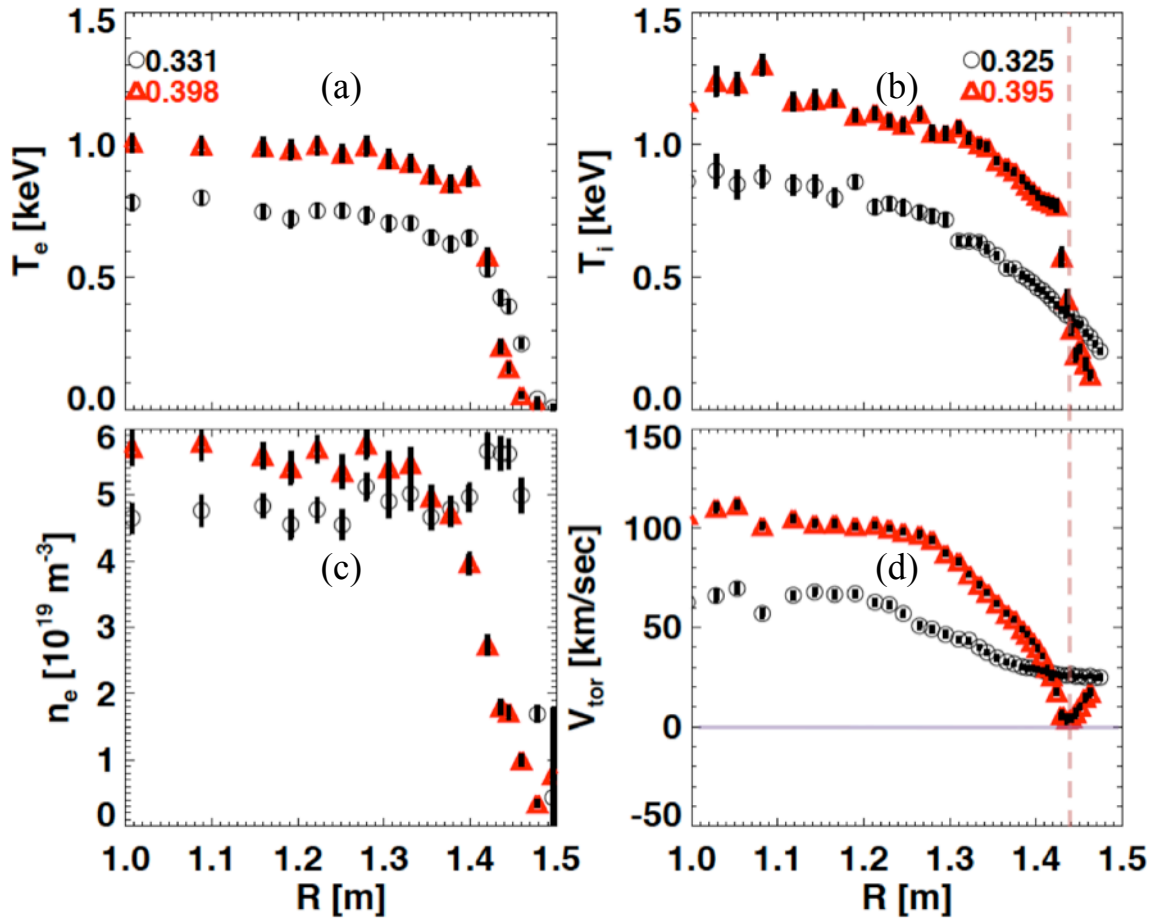

Figure N21: Profile comparison during normal H-mode (black) and EP H-mode phases (red): (a) T_e, (b) T_i, (c) n_e, (d) V_{tor} from high I_p EP H-mode.

(ELMs), either naturally occurring or those induced by applied 3D fields[72]. The increase in the pedestal T_e, T_i leads to a high pedestal pressure and relatively low pressure peaking factor, which increases the stability limit to resistive wall modes[73, 74]. Furthermore, the wider pedestals lead to high edge bootstrap currents, low inductive flux consumption, and correspondingly high non-inductive fraction.

Historically EP H-modes have been difficult to achieve reliably. However analysis of recent data has uncovered a high I_p, low q95 scenario for reliable, albeit short-lived, EP H-modes. An example of this scenario is shown in Figure N20; the EP H-mode was triggered by the first ELM at t1, and terminated at time t2. The line-average density ramp was markedly eliminated during this phase.

Figure N21 compares the plasma profiles just before the beginning and end of the EP H-mdoe phases. The characteristic increase in T_e and T_i was observed, as was a substantial drop in the edge n_e. Finally the signature change in the toroidal rotation (V_{tor}) profile, namely an increase in the edge shear with a zero crossing at the edge q=3 surface, is clearly seen.

Figure N22 shows that magnetic fluctuations were enhanced in the Mirnov data during the EP H-mode shown above. An upward chirping set of coherent modes is clearly visible in the early part of EP H-mode; in general, magnetic fluctuations increased in amplitude. In addition, density fluctuations measured by the BES diagnostic also increased. We speculate that these
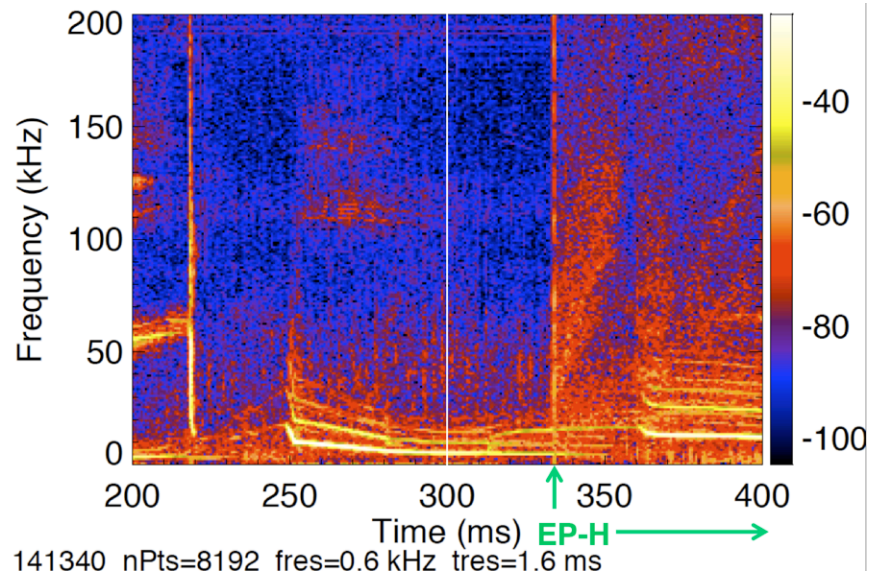

Figure N22: spectrogram of magnetic fluctuations from Mirnov data, showing increased fluctuations during EP H-mode phase.

fluctuations might be responsible for the apparent separation of particle and thermal transport channels.

Looking ahead to NSTX Upgrade, research on EP H-mode will include research on reliable triggering, and pulse length extension via β feedback. In addition, in-depth analysis of the turbulence characteristics, including comparison with the I-mode confinement regime[75, 76], is planned.

References

1   Wagner F.*, et al. Phys. Rev. Lett.* **49,** 1408(1982).
2   Zohm H. *Plasma Phys. Control. Fusion* **38,** 105(1996).
3   Loarte A.*, et al. Proc. 22nd Fusion Energy Conference, Geneva, SZ, 13-18 Oct. 2008* IT/P6(2008).
4   Connor J. W.*, et al. Phys. Plasmas* **5,** 2687(1998).
5   Snyder P. B.*, et al. Phys. Plasmas* **9,** 2037(2002).
6   Wilson H. R.*, et al. Phys. Plasmas* **9,** 1277(2002).
7   Snyder P. B.*, et al. Plasma Phys. Control. Fusion* **46,** A131(2004).
8   Maingi R.*, et al. Nucl. Fusion* **45,** 1066(2005).
9   Kirk A.*, et al. Plasma Phys. Control. Fusion* **46,** 551(2003).
10   Maingi R.*, et al. Phys. Rev. Lett.* **103,** 075001(2009).
11   Diallo A.*, et al. Nucl. Fusion* **51,** 103031(2011).
12   Snyder P. B. *Nucl. Fusion* **49,** 085035(2009).
13   LeBlanc B. P.*, et al. Rev. Sci. Instrum.* **74,** 1659(2003).
14   Bell R. E.*, et al. Phys. Plasmas* **17,** 082507(2010).
15   Lao L. L.*, et al. Nucl. Fusion* **25,** 1611(1985).
16   Sabbagh S. A.*, et al. Nucl. Fusion* **41,** 1601(2001).
17   Kirk A.*, et al. Plasma Phys. Control. Fusion* **49,** 1259(2007).
18   Maggi C. F.*, et al. Nucl. Fusion* **47,** 535(2007).
19   Groebner R. J.*, et al. Nucl. Fusion* **49,** 045013(2009).
20   Kirk A.*, et al. Plasma Phys. Control. Fusion* **51,** 065016(2009).
21   Groebner R. J.*, et al. Nucl. Fusion* **49,** 085037(2009).
22   Burckhart A.*, et al. Plasma Phys. Control. Fusion* **52,** 105010(2010).
23   Maggi C. F. *Nucl. Fusion* **50,** 066001(2010).
24   Snipes J.*, et al. J. Nucl. Mater.* **196-198,** 686(1992).
25   Mansfield D. K.*, et al. Nucl. Fusion* **41,** 1823(2001).
26   Majeski R.*, et al. Phys. Rev. Lett.* **97,** 075002(2006).
27   Apicella M.*, et al. J. Nucl. Mater.* **363-365,** 1346(2007).
28   Sánchez J.*, et al. J. Nucl. Mater.* **390-391,** 852(2009).
29   Kugel H. W.*, et al. J. Nucl. Mater.* **363-365,** 791(2007).
30   Kugel H. W.*, et al. Phys. Plasmas* **15,** 056118(2008).
31   Bell M. G.*, et al. Plasma Phys. Control. Fusion* **51,** 124054(2009).
32   Kugel H. W.*, et al. J. Nucl. Mater.* **390-391,** 1000(2009).
33   Maingi R.*, et al. Nucl. Fusion* **51,** 063036(2011).
34   Maingi R.*, et al. Nucl. Fusion* **45,** 264(2005).
35   Mansfield D. K.*, et al. J. Nucl. Mater.* **390-391,** 764(2009).
36   Boyle D. P.*, et al. Plasma Phys. Control. Fusion* **53,** 105011(2011).
37   Hawyrluk R. J. *Phys. of Plasmas Close to Thermonuclear Cond.* **1,** 19(1980).

38   Goldston R. J*., et al. J. Comput. Phys.* **43,** 61(1981).
39   Maingi R*., et al. Phys. Rev. Lett.* **107,** 145004(2011).
40   Ding S*., et al. Plasma Phys. Control. Fusion* **52,** 015001(2010).
41   Menard J. E. *Nucl. Fusion* **43,** 330(2003).
42   Sabbagh S. A. *Nucl. Fusion* **46,** 635(2006).
43   Kaye S. M., M. Greenwald, U. Stroth *Nucl. Fusion* **37,** 1303(1997).
44   Canik J. M*., et al. Nucl. Fusion* **51,** 064016(2010).
45   Canik J. M*., et al. Phys. Rev. Lett.* **104,** 045001(2010).
46   Soukhanovskii V. A*., et al. Nucl. Fusion* **51,** 012001(2011).
47   Osborne T. H*., et al. J. Phys.: Conf. Series* **123,** 012014(2008).
48   LeBlanc B. *Nucl. Fusion* **44,** 513(2004).
49   Groebner R. J*., et al. Phys. Plasmas* **5,** 1800(1998).
50   Canik J. M*., et al. J. Nucl. Mater.* **415,** S409(2011).
51   Schneider R. *Contrib. Plasma Phys.* **46,** 3(2006).
52   Reiter D. *J. Nucl. Mater.* **196-198,** 80(1992).
53   Smirnov R. D*., et al. Contributions to Plasma Physics* **50,** 299(2010).
54   Canik J. M*., et al. Phys. Plasmas* **18,** 056118(2011).
55   Soukhanovskii V. A. *Rev. Sci. Instrum.* **75,** 4320(2004).
56   Mastrovito D. M. *Rev. Sci. Instrum.* **74,** 5090(2003).
57   Maingi R*., et al. J. Nucl. Mater.* **363-365,** 196(2007).
58   Kubota S*., et al. Bull. Am. Phys. Soc.* **53,** 188(2008).
59   Jenko F*., et al. Phys. Plasmas* **8,** 4096(2001).
60   Jenko F*., et al. Phys. Plasmas* **16,** 055901(2009).
61   Ren Y*., et al. Phys. Rev. Lett.* **106,** 165005(2011).
62   Callen J. *Phys. Rev. Lett.* **94,** 055002(2005).
63   Callen J. D*., et al. Phys. Plasmas* **17,** 056113(2010).
64   Callen J. D*., et al. Phys. Rev. Lett.* submitted(2011).
65   Sauter O*., et al. Phys. Plasmas* **6,** 2834(1999).
66   Thomas D*., et al. Phys. Rev. Lett.* **93,** 2004).
67   Sontag A. C*., et al. Nucl. Fusion* **51,** 103022(2011).
68   Kaye S. M*., et al. Phys. Rev. Lett.* **98,** 175002(2007).
69   Bell R. E. *Phys. Plasma* submitted(2010).
70   Maingi R*., et al. Phys. Rev. Lett.* **105,** 135004(2010).
71   Maingi R*., et al. J. Nucl. Mater.* **390-391,** 440(2009).
72   Canik J. M*., et al. Phys. Rev. Lett.* **104,** 045001(2010).
73   Lazarus E. A*., et al. Phys. Rev. Lett.* **77,** 2714(1996).
74   Sabbagh S. A*., et al. Proc. 16th Internatonal Conf. on Fusion Energy, Montreal, CA, 7-11 Oct. 1996* AP2(1996).
75   McDermott R. M*., et al. Phys. Plasmas* **16,** 056103(2009).
76   Whyte D. G*., et al. Nucl. Fusion* **50,** 105005(2010).

Information Services
Princeton Plasma Physics Laboratory
P.O. Box 451
Princeton, NJ 08543

Phone: 609-243-2245
Fax: 609-243-2751
e-mail: pppl_info@pppl.gov
Internet Address: http://www.pppl.gov